

# Hadronic top-quark pair production in association with two jets at Next-to-Leading Order QCD

G. Bevilacqua,<sup>1</sup> M. Czakon,<sup>1</sup> C. G. Papadopoulos,<sup>2</sup> and M. Worek<sup>3</sup>

<sup>1</sup>*Institut für Theoretische Teilchenphysik und Kosmologie,  
RWTH Aachen University, D-52056 Aachen, Germany*

<sup>2</sup>*Institute of Nuclear Physics, NCSR Demokritos, GR-15310 Athens, Greece*

<sup>3</sup>*Fachbereich C, Bergische Universität Wuppertal, D-42097 Wuppertal, Germany*  
(Dated: August 16, 2011)

We report on the calculation of the next-to-leading order QCD corrections to the production of  $t\bar{t}$  pairs in association with two hard jets at the Fermilab TeVatron and CERN Large Hadron Collider. Results for the integrated and differential cross sections are given. The corrections with respect to leading order are negative and moderate. A study of the scale dependence of our NLO predictions indicates that the residual theoretical uncertainty, due to higher order corrections, is 21% for the TeVatron and 15% for the LHC. In case of the TeVatron, the forward-backward asymmetry of the top quark is calculated for the first time at next-to-leading order. With the inclusive selection of cuts, this asymmetry amounts to  $\mathcal{A}_{\text{FB,LO}}^t = -10.3\%$  at leading order and  $\mathcal{A}_{\text{FB,NLO}}^t = -4.6\%$  at next-to-leading order. All results presented in this paper have been obtained with the help of the HELAC-NLO package.

PACS numbers: 12.38.Bx, 14.65.Ha, 14.80.Bn

## I. INTRODUCTION

Top quark production in association with two jets constitutes an important background for many new particle searches at the Tevatron and at the LHC. Prominent examples include searches for Higgs boson decays  $H \rightarrow WW^*$  and  $H \rightarrow b\bar{b}$ , where the Higgs boson is produced via weak boson fusion or via an associated production with a  $t\bar{t}$  pair respectively. Higgs boson production in association with top quarks has a strongly decreasing cross section with increasing Higgs boson mass, which makes the process useful only in the low mass range,  $m_H \leq 135$  GeV, when Higgs boson decays in  $b\bar{b}$  are important. This potential discovery channel gives a unique access to the top and bottom Yukawa couplings. Combined analyses of ATLAS [1] and CMS [2] have shown that a  $3\sigma$  evidence of the signal above the dominant  $t\bar{t}b\bar{b}$  and  $t\bar{t}jj$  backgrounds can be obtained for  $M_H \leq 130$  GeV at the LHC, if enough luminosity,  $\mathcal{L} = 60 \text{ fb}^{-1}$ , is collected. However, a reconstruction of the  $H \rightarrow b\bar{b}$  mass peak is difficult because of an identification problem in the signal. The  $b\bar{b}$  pair can be chosen incorrectly, due to a lack of a distinctive kinematic feature of jets from the Higgs boson decay. Moreover, the b-tagging efficiency takes a crucial part in this kind of analyzes, since two b-jets for a Higgs boson candidate can arise from mistagged light jets. Therefore, a very precise knowledge of the backgrounds is necessary, if the  $t\bar{t}H$  channel is to be of any use.

On the other hand, a detailed ATLAS examination of the vector boson fusion channel at the LHC,  $pp \rightarrow Hjj \rightarrow W^+W^-jj \rightarrow \ell\nu\ell\nu jj$ , has shown that a significance larger than  $3\sigma$  can be obtained for a luminosity of  $\mathcal{L} = 10 \text{ fb}^{-1}$  in the Higgs boson mass range above  $m_H \sim 130$  GeV, *i.e.* when  $\mathcal{BR}(H \rightarrow WW^*)$  is large enough [3]. When combining this channel with the  $\ell\nu jj$  mode, one

can even obtain a  $\sim 5\sigma$  significance for the above mass range. In fact, the  $pp \rightarrow Hjj \rightarrow WWjj$  channel becomes very powerful at higher Higgs boson masses. One can arrive at a signal significance that is above  $5\sigma$  in a wide mass range, namely from 140 GeV up to 190 GeV, for the same luminosity. Although feasible and competitive, this channel might prove to be rather difficult since the Higgs boson mass peak cannot be directly reconstructed. Consequently, one cannot measure background processes from the side bands. The most important background processes,  $t\bar{t}jj$  and QCD  $W^+W^-jj$ , need to be known, therefore, as precisely as possible.

Meanwhile at the TeVatron, with up to  $7.1 \text{ fb}^{-1}$  of data analyzed at CDF, and up to  $8.2 \text{ fb}^{-1}$  at D0, the Higgs boson mass range of  $158 \text{ GeV} < m_H < 173 \text{ GeV}$  has been excluded [4]. Very recently, the LHC experiments have presented their Higgs boson search results based on  $1 \text{ fb}^{-1}$  of analyzed data. CMS has excluded the Standard Model Higgs boson in the 149 GeV – 206 GeV and 300 GeV – 440 GeV windows [5], while ATLAS has excluded the 155 GeV – 190 GeV and 295 GeV – 450 GeV windows [6]. The low mass exclusion is dominated by the search of the  $H \rightarrow W^+W^- \rightarrow \ell\nu\ell\nu$  final state, while the high mass one is dominated by  $H \rightarrow ZZ$  with three different combinations of Z decays. Considering these recent experimental results, an excellent understanding of lighter Higgs boson search channels is more timely than ever.

Apart from its significance as a background process to various new physics searches it turns out that  $t\bar{t}jj$  production can also be an important signal process. With the total integrated luminosity accumulated so far at the TeVatron around 3000 events should have been collected so far by each experiment. As for the LHC, in June of this year both experiments ATLAS and CMS reached  $1 \text{ fb}^{-1}$  of collected data. This can be directly translated to about

10000 events already stored. Since they are in the process of collecting data, the  $t\bar{t}jj$  process can soon become of great importance for a more precise understanding of the top quark events topology.

However, it is a well known fact that for processes involving strongly interacting particles, the leading order (LO) cross sections are affected by large uncertainties arising from higher order corrections. If, at least, next-to-leading order (NLO) QCD corrections to these processes are included, total cross sections can be defined in a reliable way. The NLO QCD corrections to  $pp \rightarrow t\bar{t}b\bar{b}$  production have already been calculated by two independent groups [7–9], and perfect agreement has been found. In addition, NLO corrections to the remaining two background processes, namely  $pp \rightarrow W^+W^-jj$  [10] and  $pp \rightarrow t\bar{t}jj$  [11] have recently been evaluated. In this paper, we have extend our previous study on the NLO QCD corrections to the  $pp \rightarrow t\bar{t}jj$  production at the LHC, where the integrated cross section together with the scale dependence of the total cross section for one particular set of cuts for the center of mass system energy of  $\sqrt{s} = 14$  TeV have been studied. Moreover, we have presented there three differential distributions, the invariant mass distribution of the first and the second hardest jet together with the transverse momentum distributions of the first and the second hard jet. We supplement this discussion here with more results. In particular, results for the TeVatron case are going to be presented for the first time. In case of the LHC, we use the current center of mass system energy of  $\sqrt{s} = 7$  GeV. Additionally to the integrated cross sections for different setups, various differential distributions are given.

The article is organized as follows. In Section II we briefly summarize the methods we use to obtain our NLO QCD results. In Section III numerical results are presented, first for the TeVatron and later on for the LHC case. We give our conclusions in Section IV. Finally, in an Appendix we give values of squared matrix elements for the virtual corrections for one phase space point.

## II. FRAMEWORK OF THE CALCULATION

The calculation of NLO corrections to hadronic top pair production in association with two jets proceeds along the same lines as our earlier work on  $pp \rightarrow t\bar{t}b\bar{b}$  [8],  $pp \rightarrow t\bar{t}jj$  [11] and  $pp(p\bar{p}) \rightarrow t\bar{t} \rightarrow W^+W^-b\bar{b} \rightarrow e^+\nu_e\mu^-\bar{\nu}_\mu b\bar{b}$  [12]. The methods developed there have therefore been straightforwardly adapted and only need a brief recollection here. Let us emphasize, that all parts of the calculation are performed fully numerically in a completely automatic manner.

### A. Tree level contributions

At tree level the  $t\bar{t}$  production in association with two jets proceeds via the scattering of two gluons, two

TABLE I. *Partonic subprocesses contributing to the leading order process  $pp(p\bar{p}) \rightarrow t\bar{t}jj$  at  $\mathcal{O}(\alpha_s^4)$ . The number of Feynman diagrams corresponding to these subprocesses is also shown.*

PARTONIC SUBPROCESS	NUMBER OF FEYNMAN DIAGRAMS
$gg \rightarrow t\bar{t}gg$	123
$gg \rightarrow t\bar{t}q\bar{q}$	36
$q\bar{q} \rightarrow t\bar{t}gg$	36
$gq \rightarrow t\bar{t}qg$	36
$qg \rightarrow t\bar{t}qg$	36
$qq' \rightarrow t\bar{t}qq'$	7
$q\bar{q} \rightarrow t\bar{t}q'\bar{q}'$	7
$q\bar{q} \rightarrow t\bar{t}q\bar{q}$	14

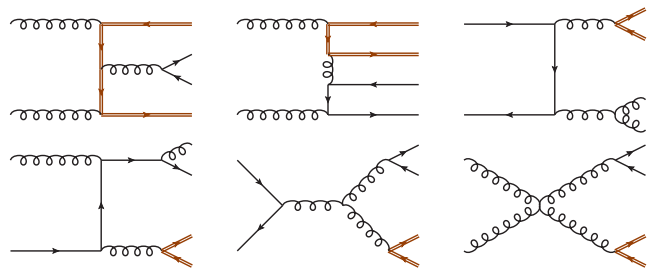


FIG. 1. *A representative set of Feynman diagrams contributing to the LO hadronic  $t\bar{t}jj$  production at  $\mathcal{O}(\alpha_s^4)$ . Double brown lines correspond to top quarks, single lines to light quarks and wiggly ones to gluons.*

quarks or quark and gluon. All contributions of the order of  $\mathcal{O}(\alpha_s^4)$  can be grouped into eight easily identifiable topologies presented in the Table I. Both  $q$  and  $q'$  span all quarks and anti-quarks. Also shown are the numbers of Feynman diagrams corresponding to these subprocesses. We emphasize here that we do not use Feynman diagrams in our calculations. Instead, matrix elements and total cross sections are obtained with an iterative algorithm based on the Dyson-Schwinger equations [13, 14]. Nevertheless, we present the number of Feynman diagrams as a measure of complexity. All partonic channels have been calculated with the HELAC-DIPOLES [15] package. An independent calculation using the HELAC-PHEGAS [16–18] event generator has been performed. Let us stress that HELAC-PHEGAS has been already extensively used and tested, see *e.g.* [19–24]. Moreover, both libraries compute relevant contributions in a very efficient way, using off-shell recursive equations and avoiding a multiple evaluation of recurring building blocks. In every case we have found full numerical agreement. The optimization and phase space integration was executed with the help of PARNI [25] and KALEU [26]. A few examples of LO graphs are shown in Figure 1.

TABLE II. The number of one-loop Feynman diagrams for the  $pp(p\bar{p}) \rightarrow t\bar{t}jj$  process at  $\mathcal{O}(\alpha_s^5)$ .

PARTONIC SUBPROCESS	NUMBER OF FEYNMAN DIAGRAMS
$gg \rightarrow t\bar{t}gg$	4510
$gg \rightarrow t\bar{t}q\bar{q}$	1100
$q\bar{q} \rightarrow t\bar{t}gg$	1100
$gq \rightarrow t\bar{t}qg$	1100
$qg \rightarrow t\bar{t}qg$	1100
$qq' \rightarrow t\bar{t}qq'$	205
$q\bar{q} \rightarrow t\bar{t}q'\bar{q}'$	205
$q\bar{q} \rightarrow t\bar{t}q\bar{q}$	410

### B. Virtual corrections

The virtual corrections are obtained from the interference of the sum of all one-loop diagrams with the Born amplitude. One can classify them into self-energy, vertex, box-type, pentagon-type and hexagon-type corrections. In Table II the number of one-loop Feynman diagrams for the  $pp(p\bar{p}) \rightarrow t\bar{t}jj$  process at  $\mathcal{O}(\alpha_s^5)$  as obtained with QGRAPH [27] is given. Again they are shown as a measure of complexity of our calculation since we are free from the task of computing Feynman graphs for a given process. Typical examples of virtual graphs are shown in Figure 2. The virtual corrections are calculated in  $d = 4 - 2\epsilon$  dimensions in the 't Hooft-Veltman [28] version of the dimensional regularization scheme. The singularities stemming from infrared divergent pieces are canceled by the respective poles in the integrated counter terms of the dipole subtraction approach. The finite contributions of the loop diagrams are evaluated numerically in  $d = 4$  dimension. We monitor the numerical stability by checking Ward identities at every phase space point. The events which violate gauge invariance are not discarded from the calculation of the finite part, but rather recalculated with higher precision. In order to compute the relevant contributions the HELAC-1LOOP [29] approach is used. It is based on the HELAC-PHEGAS program to calculate all tree-order like ingredients and the OPP [30] reduction method. The cut-constructible part of the virtual amplitudes and of the rational terms,  $R_1$ , are computed using the CUTTOOLS [31] code. The remaining part of the rational term,  $R_2$ , is obtained by the use of extra Feynman rules as described in [31–35]. The evaluation of scalar integrals is performed with the help of ONELOOP [29, 36]. Renormalization is done as usual, by evaluating tree level diagrams with counterterms. For our process, we chose to renormalize the coupling in the  $\overline{\text{MS}}$  scheme with five active flavors and the top quark decoupled, just as in [8, 11], and the mass in the on-shell scheme (wave function renormalization is done in the on-shell scheme as it must be).

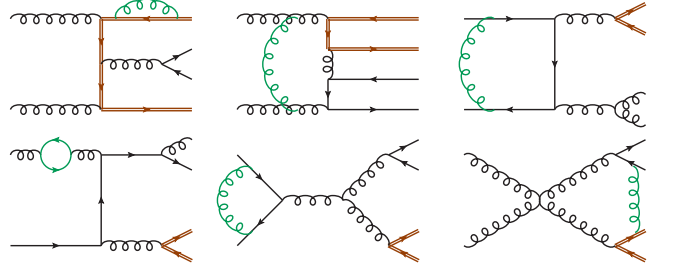


FIG. 2. A representative set of Feynman diagrams contributing to the virtual corrections to hadronic  $t\bar{t}jj$  production at  $\mathcal{O}(\alpha_s^5)$ . Double brown lines correspond to top quarks, single lines to light quarks and wiggly ones to gluons.

TABLE III. Partonic subprocesses contributing to the subtracted real emissions at  $\mathcal{O}(\alpha_s^5)$  for the  $pp(p\bar{p}) \rightarrow t\bar{t}jj$  process. Also, the number of Feynman diagrams and the number of dipoles corresponding to these subprocesses are presented.

PARTONIC SUBPROCESS	NUMBER OF FEYNMAN DIAGRAMS	NUMBER OF DIPOLES
$gg \rightarrow t\bar{t}ggg$	1240	75
$gg \rightarrow t\bar{t}q\bar{q}g$	341	55
$q\bar{q} \rightarrow t\bar{t}ggg$	341	75
$gq \rightarrow t\bar{t}q'\bar{q}'q$	64	25
$gq \rightarrow t\bar{t}q\bar{q}g$	341	65
$qg \rightarrow t\bar{t}q'\bar{q}'q$	64	25
$qg \rightarrow t\bar{t}q\bar{q}g$	341	65
$qq' \rightarrow t\bar{t}qq'g$	64	40
$q\bar{q} \rightarrow t\bar{t}q'\bar{q}'g$	64	35
$q\bar{q} \rightarrow t\bar{t}q\bar{q}g$	128	45

### C. Real corrections

The real emission corrections to the LO process arise from tree level amplitudes with one additional parton, an additional gluon, or a quark anti-quark pair replacing a gluon. All possible contributions of the order of  $\mathcal{O}(\alpha_s^5)$  can be divided into ten subprocesses which are given in Table III, where again  $q$  and  $q'$  stand for up- or down-type quarks. Moreover, the number of Feynman diagrams and the number of dipoles corresponding to these partonic reactions are shown. We employ the dipole subtraction formalism in the form as proposed by Catani and Seymour [37], to extract the soft and collinear infrared singularities and to combine them with the virtual corrections. Specifically, the formulation presented in [38] for massive quarks has been used with the extension to arbitrary helicity eigenstates of the external partons [15], as implemented in HELAC-DIPOLES. After combining virtual and real corrections, singularities connected to collinear configurations in the final state as well as soft divergences in the initial and final states cancel

for collinear-safe observables automatically after applying a jet algorithm. Singularities connected to collinear initial-state splittings are removed via factorization by parton distribution function redefinitions. In our case the cancellation of divergences has been checked numerically for a few phase space points. Let us mention here that similarly to the LO case, the phase space integration is executed with the help of KALEU [26]. However, in case of subtracted real emission a version with dipoles channels have been used instead, see [12] for details.

### III. NUMERICAL RESULTS

In the following we present predictions for the process  $p\bar{p}(pp) \rightarrow t\bar{t}jj + X$  both at the TeVatron run II with  $\sqrt{s} = 1.96$  TeV and at the Large Hadron Collider (LHC) with  $\sqrt{s} = 7$  TeV. We have consistently employed the MSTW2008 [39] set of parton distribution functions (PDFs). In particular, we take MSTW2008LO PDFs with 1-loop running  $\alpha_s$  in LO and MSTW2008NLO PDFs with 2-loop running  $\alpha_s$  in NLO, including five active flavors. Contributions induced by bottom-quark density are taken into account. We use the Tevatron average mass of the top quark  $m_t = 173.3$  GeV [40] as measured by the CDF and D0 experiments. The masses of all other quarks, including b quarks, are neglected. If not stated otherwise, the renormalization and factorization scales are set to  $\mu_R = \mu_F = m_t$ . Jets are defined via an infrared safe algorithm, the  $k_T$  [41–43], *anti*- $k_T$  [44] (our default) and the inclusive Cambridge/Aachen (C/A) algorithm [45]. In all cases no clustering can take place unless two partons of pseudorapidity

$$|\eta| = -\ln[\tan(\theta/2)] < 5, \quad (1)$$

where  $\theta$  is the angle between the parton momentum and the beam axis, are separated by less than  $R$  in the  $(\eta, \phi)$  plane. Reconstructed jets are ordered in  $p_T$ . Their momenta are formed as the four-vector sum of massless partons. The outgoing (anti-)top quarks are left on-shell with unrestricted kinematics. They are assumed to be always tagged.

#### A. TeVatron

We calculate the partonic cross sections for events with at least two hard jets. Jets are obtained via the *anti*- $k_T$  jet algorithm with a resolution parameter  $R = 0.4$  and are required to have

$$p_{T_j} = \sqrt{p_{x_j}^2 + p_{y_j}^2} > 20 \text{ GeV}, \quad (2)$$

$$|y_j| = \frac{1}{2} \ln \left( \frac{E_j + p_{z_j}}{E_j - p_{z_j}} \right) < 2, \quad (3)$$

TABLE IV. *Integrated cross section at LO and NLO for  $p\bar{p} \rightarrow t\bar{t}jj + X$  production at the TeVatron run II with  $\sqrt{s} = 1.96$  TeV. Results for three different jet algorithms are presented, the anti- $k_T$ ,  $k_T$  and the Cambridge/Aachen jet algorithms with  $R = 0.4$ . The scale choice is  $\mu_R = \mu_F = m_t$ .*

CUTS	$\sigma_{\text{LO}}$ [pb]	$\sigma_{\text{NLO}}^{\text{anti-}k_T}$ [pb]	$\sigma_{\text{NLO}}^{k_T}$ [pb]	$\sigma_{\text{NLO}}^{\text{C/A}}$ [pb]
$p_{T_j} > 20 \text{ GeV}$				
$\Delta R_{jj} > 0.4$	0.3584(1)	0.2709(5)	0.2734(4)	0.2734(4)
$ y_i  < 2.0$				

TABLE V. *Integrated cross section at LO and NLO for  $p\bar{p} \rightarrow t\bar{t}jj + X$  production at the TeVatron run II with  $\sqrt{s} = 1.96$  TeV. Results for three different jet algorithms are presented, the anti- $k_T$ ,  $k_T$  and the Cambridge/Aachen jet algorithms with  $R = 0.8$ . The scale choice is  $\mu_R = \mu_F = m_t$ .*

CUTS	$\sigma_{\text{LO}}$ [pb]	$\sigma_{\text{NLO}}^{\text{anti-}k_T}$ [pb]	$\sigma_{\text{NLO}}^{k_T}$ [pb]	$\sigma_{\text{NLO}}^{\text{C/A}}$ [pb]
$p_{T_j} > 20 \text{ GeV}$				
$\Delta R_{jj} > 0.8$	0.2876(1)	0.2467(3)	0.2494(3)	0.2491(3)
$ y_j  < 2.0$				

$$\Delta R_{jj} = \sqrt{\Delta\phi_{jj}^2 + \Delta y_{jj}^2} > 0.4. \quad (4)$$

We will refer to this set of cuts as *TeVatron default selection*. All results presented in this Section are given in picobarns, except for the Table VII, where results are shown in femtobarns.

#### 1. Integrated cross sections

Now we turn to a discussion of the numerical results. We start with the total cross sections for the TeVatron default selection. We find

$$\sigma_{\text{LO}}^{\text{TeV}}(pp \rightarrow t\bar{t}jj) = 0.3584^{+0.3390(94\%)}_{-0.1606(45\%)} \text{ pb}, \quad (5)$$

$$\sigma_{\text{NLO}}^{\text{TeV}}(pp \rightarrow t\bar{t}jj) = 0.2709^{+0.0014(0.5\%)}_{-0.0566(21\%)} \text{ pb}. \quad (6)$$

TABLE VI. *Integrated cross section at NLO for  $p\bar{p} \rightarrow t\bar{t}jj + X$  production at the TeVatron run II with  $\sqrt{s} = 1.96$  TeV. Results for two different values of the  $\alpha_{\text{max}}$  parameter, jet resolution  $R$  and  $\Delta R_{jj}$  cut for the anti- $k_T$  jet algorithm are presented. The scale choice is  $\mu_R = \mu_F = m_t$ .*

CUTS	$\sigma_{\text{NLO}}^{\alpha_{\text{max}}=0.01}$ [pb]	$\sigma_{\text{NLO}}^{\alpha_{\text{max}}=1.00}$ [pb]
$\Delta R_{jj} > 0.4, R = 0.4$	0.2709(5)	0.2710(2)
$\Delta R_{jj} > 0.8, R = 0.8$	0.2467(3)	0.2466(2)

TABLE VII. Integrated cross section at LO and NLO for  $p\bar{p} \rightarrow t\bar{t}jj + X$  production at the TeVatron run II with  $\sqrt{s} = 1.96$  TeV. Results for the anti- $k_T$  jet algorithm with  $R = 0.4$  are presented. In the last two columns the  $\mathcal{K}$  factor, defined as the ratio of the NLO cross section to the respective LO result, and NLO corrections in % are given. The scale choice is  $\mu_R = \mu_F = m_t$ .

$p_{T_j}$ CUT	$\sigma_{\text{LO}}$ [fb]	$\sigma_{\text{NLO}}^{\text{anti-}k_T}$ [fb]	$\mathcal{K}$	[%]
$p_{T_j} > 20$ GeV	358.4(1)	271.2(4)	0.76	-24
$p_{T_j} > 40$ GeV	79.29(3)	54.11(9)	0.68	-32
$p_{T_j} > 60$ GeV	23.85(1)	14.55(3)	0.61	-39
$p_{T_j} > 80$ GeV	8.274(3)	4.520(13)	0.55	-45

At the central value of the scale,  $\mu_R = \mu_F = m_t$ , the full cross section receives moderate NLO correction of the order of  $-24\%$ . The scale dependence is indicated by the upper and lower indices. The upper (lower) index represents the change when the scale is shifted towards  $\mu = m_t/2$  ( $\mu = 2m_t$ ). Rescaling the common scale from the default value  $m_t$  up and down by a factor 2 changes the cross section at LO by about 94%. Through the inclusion of NLO QCD corrections the scale uncertainty is dramatically reduced down to 21%.

To assess the effect of changing the jet algorithm, we compare NLO results for the  $k_T$ , anti- $k_T$  and the inclusive Cambridge/Aachen (C/A) jet algorithms as presented in Table IV. With the jet resolution parameter of  $R = 0.4$  the difference is within 1%. Total cross sections with a higher jets separation cut,  $\Delta R_{jj} > 0.8$ , and the jet resolution parameter  $R = 0.8$  are shown in Table V. The NLO QCD corrections are reduced down to  $-16\%$  in that case. This is mostly due to a large,  $-20\%$  change, in the LO cross section as compared to a rather moderate,  $-9\%$  shift at NLO. With an increase of the  $R$  parameter the perturbative difference between the algorithms should be more visible because the phase space for inclusion of an extra parton in the jet is much larger. Nevertheless in our case it remains within 1%.

For completeness and as part of checks, the integrated NLO cross sections for two different values of the  $\alpha_{\text{max}}$  parameter are given in Table VI. Let us remind the reader that the  $\alpha_{\text{max}}$  parameter is a common modification of subtraction terms in the phase space away from the singularity. We consider two extreme choices, namely  $\alpha_{\text{max}} = 1$ , which corresponds to the original formulation of [38], and  $\alpha_{\text{max}} = 0.01$ . As can be observed, the independence of the final result on the value of  $\alpha_{\text{max}}$  is obtained at the permil level.

In Table VII we provide LO and NLO predictions for the integrated cross sections for the TeVatron default selection, however, for different values of the transverse momentum cut for the first and the second hardest jet. The values are given for the central scale value  $\mu_R = \mu_F = m_t$ . Up to  $\sim 50$  GeV, rather moderate cor-

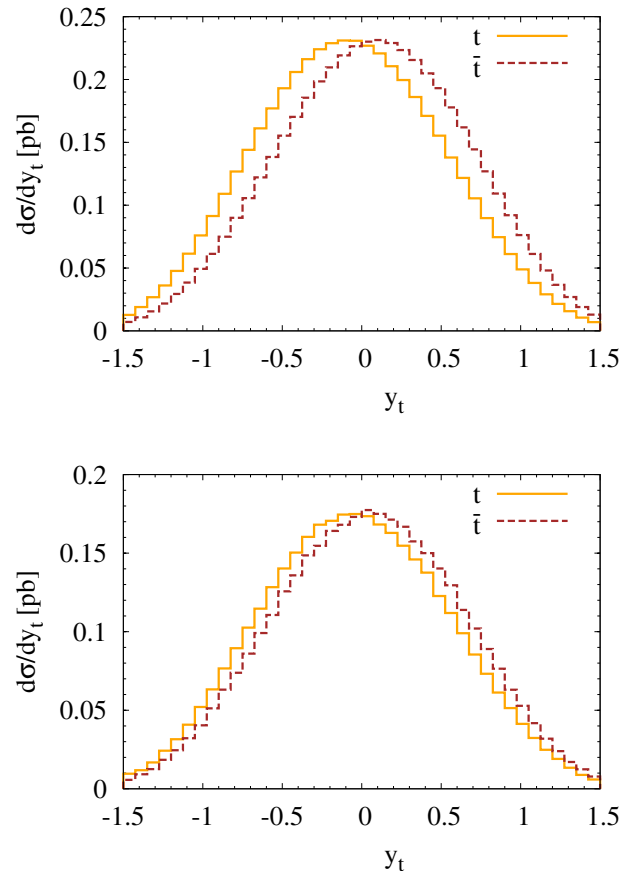


FIG. 3. Differential cross section distributions as a function of rapidity,  $y_t$ , of the top and anti-top quark at LO (upper panel) and NLO (lower panel) for  $p\bar{p} \rightarrow t\bar{t}jj + X$  production at the TeVatron run II with  $\sqrt{s} = 1.96$  TeV. The (orange) solid curve corresponds to the top quark, whereas the (brown) dashed one to the anti-top quark.

rections are acquired, however, for the high value of  $p_{T_j}$  cut, a substantial increase is noticed. For a  $p_{T_j}$  change by a factor of 4, NLO QCD corrections are almost doubled. Compared to the total NLO  $t\bar{t}$  cross section,

$$\sigma_{\text{NLO}}^{\text{TeV}}(p\bar{p} \rightarrow t\bar{t}) = 6.68^{+0.35(5.2\%)}_{-0.75(11.2\%)} \text{ pb}, \quad (7)$$

obtained for the same setup, we find that for the small  $p_{T_j}$  cut of 20 GeV the  $t\bar{t}jj$  events represent only 4% of the total cross section. The fraction is reduced substantially, down to 0.8%, 0.2% and 0.07% respectively, if a  $p_{T_j}$  cut of 40 GeV, 60 GeV and 80 GeV is chosen instead.

## 2. Forward-Backward Asymmetry

In the next step we calculate the top quark forward-backward asymmetry. At LO the asymmetry is defined

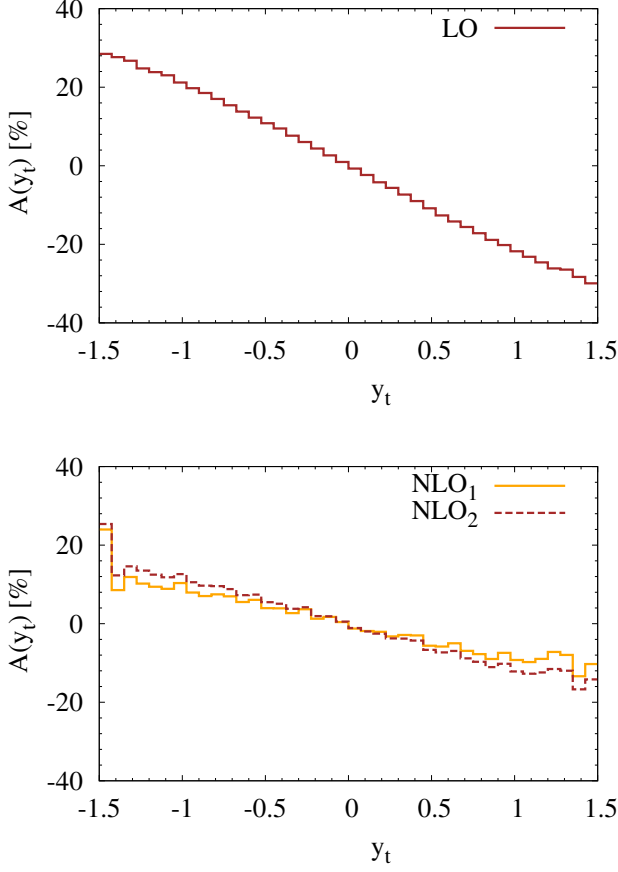


FIG. 4. Differential charge asymmetry,  $A(y_t)$ , as a function of the (anti-)top quark rapidity at LO (upper panel) and NLO (lower panel) for  $p\bar{p} \rightarrow t\bar{t}jj + X$  production at the Tevatron run II with  $\sqrt{s} = 1.96$  TeV.  $NLO_1$  refers to a result with a consistent expansion in  $\alpha_s$ , while  $NLO_2$  to the unexpanded one.

as

$$\mathcal{A}_{\text{FB,LO}}^t = \frac{\sigma_{\text{LO}}(y_t > 0) - \sigma_{\text{LO}}(y_t < 0)}{\sigma_{\text{LO}}(y_t > 0) + \sigma_{\text{LO}}(y_t < 0)}, \quad (8)$$

where  $\sigma_{\text{LO}}^\pm = \sigma_{\text{LO}}(y_t > 0) \pm \sigma_{\text{LO}}(y_t < 0)$  is evaluated with LO PDFs and LO  $\alpha_s$ . On the other hand, the asymmetry at NLO is defined by

$$\mathcal{A}_{\text{FB,NLO}}^t = \frac{\sigma_{\text{LO}}^- + \delta\sigma_{\text{NLO}}^-}{\sigma_{\text{LO}}^+ + \delta\sigma_{\text{NLO}}^+}, \quad (9)$$

where  $\delta\sigma_{\text{NLO}}^\pm$  are the NLO contributions to the cross sections and  $\sigma_{\text{LO}}^\pm$  are evaluated with NLO PDFs and NLO  $\alpha_s$ . In case of large differences between the LO and NLO asymmetries, it is necessary to expand Eq. (9) to first order in  $\alpha_s$ . Indeed, the ratio in Eq. (9) generates contributions of  $\mathcal{O}(\alpha_s^2)$  and higher, which are affected by the unknown next-to-next-to-leading order contributions. The following definition has been used, for the same reasons,

in [46, 47]

$$\mathcal{A}_{\text{FB,NLO}}^t = \frac{\sigma_{\text{LO}}^-}{\sigma_{\text{LO}}^+} \left( 1 + \frac{\delta\sigma_{\text{NLO}}^-}{\sigma_{\text{LO}}^-} - \frac{\delta\sigma_{\text{NLO}}^+}{\sigma_{\text{LO}}^+} \right). \quad (10)$$

The size of the forward-backward asymmetry of the top quark at LO for  $t\bar{t}jj$  production amounts to

$$\mathcal{A}_{\text{FB,LO}}^t = -0.103^{+0.003}_{-0.004}. \quad (11)$$

The NLO correction to the asymmetry as calculated from Eq. (9), and with a consistent expansion in  $\alpha_s$  reads

$$\mathcal{A}_{\text{FB,NLO}}^t = -0.046^{+0.005}_{-0.006}. \quad (12)$$

Had we used an unexpanded ratio of the NLO cross sections, the result would rather be

$$\mathcal{A}_{\text{FB,NLO}}^t = -0.058^{+0.014}_{-0.042}, \quad (13)$$

which means that the two definitions give reasonably consistent results for the central scale. However, the theoretical error as calculated from the scale dependence is almost as large as the asymmetry itself in the latter case.

In Figure 3 rapidity distributions for the top and anti-top quarks are presented at LO and NLO. In both cases results are not symmetric around  $y_t = 0$  and are shifted to a larger  $y_t$  for the anti-top quarks and smaller  $y_t$  for the top quarks. This shows that anti-top quarks are preferentially emitted in the direction of the incoming protons (forward direction by definition), as implied by the sign in Eq. 12. In Figure 4, we have also plotted the differential charge asymmetry,  $\mathcal{A}(y_t)$ . In the NLO case both results with and without a consistent expansion in  $\alpha_s$  are shown. In both cases, it is clearly visible that the forward-backward asymmetry of top quarks in  $t\bar{t}jj$  production is significantly reduced if NLO QCD corrections are taken into account.

### 3. Differential cross sections

In addition to the normalization of the integrated cross section, radiative corrections can affect the shape of various kinematic distributions. To quantify the size of these distortions we have tested a variety of differential distributions.

We start in Figure 5 with the differential distribution in the rapidity of the top and anti-top,  $y_t$ , and in Figure 6 with an averaged transverse momentum of the top and anti-top quarks. The dash-dotted curve corresponds to the LO, whereas the solid one to the NLO result. The upper panels show the distributions themselves and additionally include the scale-dependence bands obtained with a scale variation by a factor of two. The lower panels display the ratio of the NLO value to the LO result, for the central scale values of  $\mu = \mu_R = \mu_F = m_t$ , called the differential  $\mathcal{K}$  factor. For the angular distributions we observe negative corrections of the order of 15% – 30%.



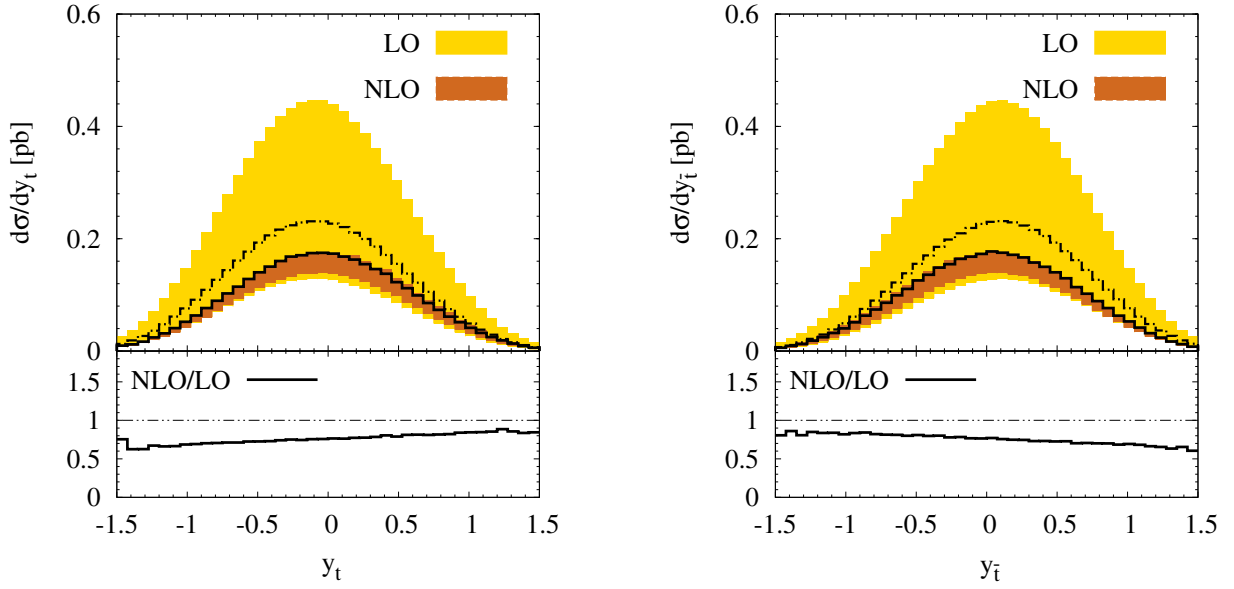


FIG. 5. Differential cross section distributions as a function of the rapidity of the top (left panel) and anti-top (right panel) for  $p\bar{p} \rightarrow t\bar{t}jj + X$  production at the TeVatron run II with  $\sqrt{s} = 1.96$  TeV. The dash-dotted curve corresponds to the LO, whereas the solid one to the NLO result. The uncertainty bands depict scale variation. The lower panels display the differential  $K$  factor.

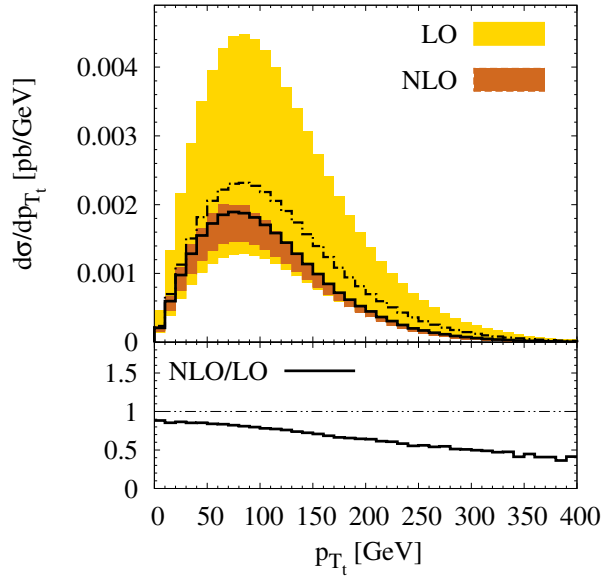


FIG. 6. Differential cross section distributions as a function of the averaged transverse momentum of the (anti-)top for  $p\bar{p} \rightarrow t\bar{t}jj + X$  production at the TeVatron run II with  $\sqrt{s} = 1.96$  TeV. The dash-dotted curve corresponds to the LO, whereas the solid one to the NLO result. The uncertainty bands depict scale variation. The lower panels display the differential  $K$  factor.

More precisely, 15% corrections are observed in the forward (backward) regions of a top (anti-top) distribution while 30% corrections are in the backward (forward) regions. For the transverse momentum distribution up to

100 GeV moderate and negative corrections of the order of 20% are reached while the tail exhibits even  $-60\%$  corrections.

In Figure 7 and Figure 8 differential cross section distributions as a function of rapidity,  $y_{t\bar{t}}$ , transverse momentum,  $p_{T_{t\bar{t}}}$ , and invariant mass,  $m_{t\bar{t}}$ , of the  $t\bar{t}$  pair are presented. Also shown is the differential distribution in the total transverse energy of the system,  $H_T$ . The latter is defined as

$$H_T = m_{T_t} + m_{T_{\bar{t}}} + \sum_{i=1,2} p_{T_{j_i}}, \quad (14)$$

where

$$m_{T_t} = \sqrt{m_t^2 + p_{T_t}^2}. \quad (15)$$

The rapidity distribution of the  $t\bar{t}$  pair has almost constant, negative and moderate 20% – 25% corrections. Both,  $m_{t\bar{t}}$  and  $p_{T_{t\bar{t}}}$  distributions get large negative 50% – 60% corrections for the higher values of these observables, which have to be compared with also negative, but 20% – 25% corrections close to the  $t\bar{t}$  threshold for  $m_{t\bar{t}}$  and for smaller values of the transverse momentum of the  $t\bar{t}$  pair for the  $p_{T_{t\bar{t}}}$  distribution. At the begin of the  $H_T$  spectrum negative and small 10% – 15% corrections can be seen. However, at the same time even  $-70\%$  can be reached for higher values.

In the next step, the jet kinematics is presented. We start with transverse momentum and rapidity distributions of the 1<sup>st</sup> and the 2<sup>nd</sup> hardest jet as depicted in Figure 9 and Figure 10. Again, in case of rapidity distributions, negative and almost constant 20% – 25% corrections are obtained. On the other hand, also negative

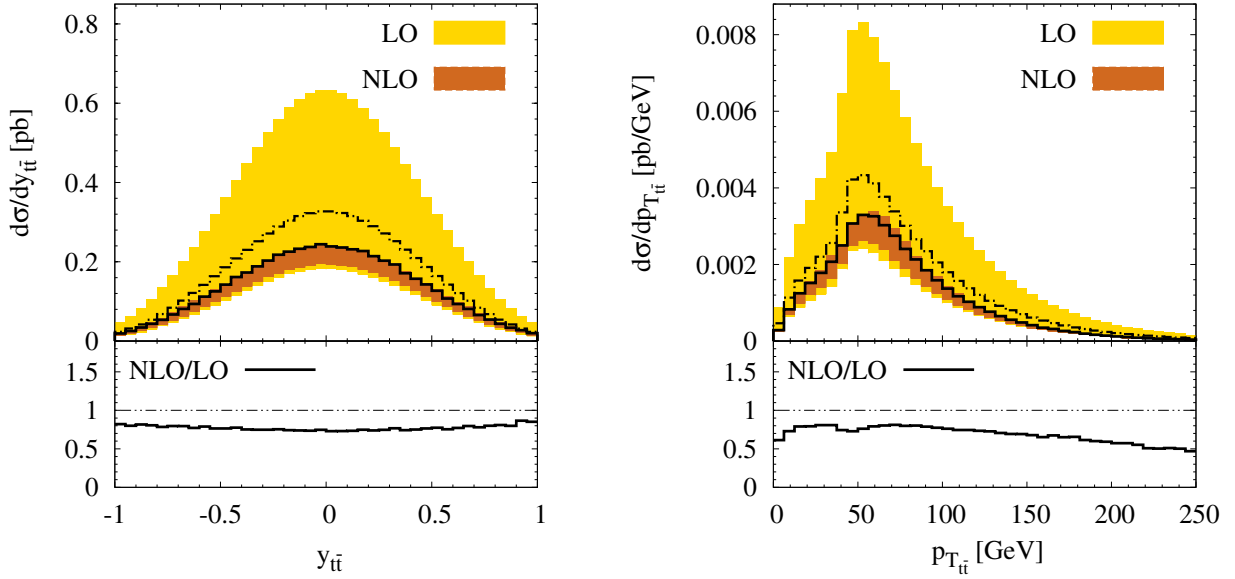


FIG. 7. Differential cross section distributions as a function of rapidity (left panel) and transverse momentum (right panel) of the  $t\bar{t}$  pair for  $p\bar{p} \rightarrow t\bar{t}jj + X$  production at the TeVatron run II with  $\sqrt{s} = 1.96$  TeV. The dash-dotted curve corresponds to the LO, whereas the solid one to the NLO result. The uncertainty bands depict scale variation. The lower panels display the differential  $\mathcal{K}$  factor.

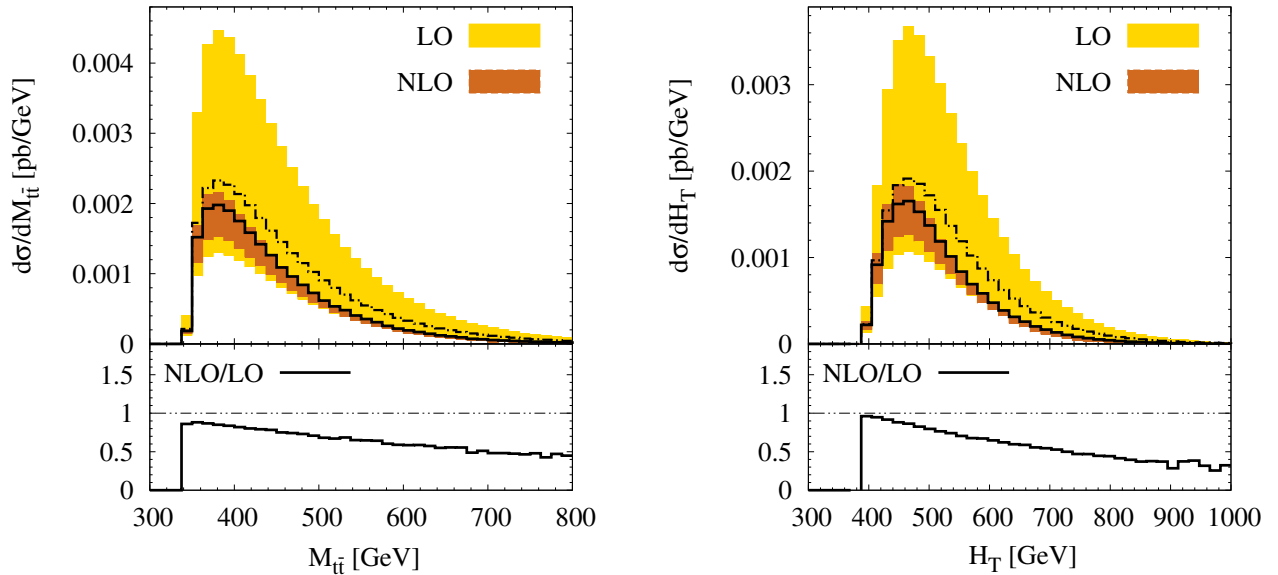


FIG. 8. Differential cross section distributions as a function of the invariant mass of the  $t\bar{t}$  pair (left panel) and of the total transverse energy (right panel) for  $p\bar{p} \rightarrow t\bar{t}jj + X$  production at the TeVatron run II with  $\sqrt{s} = 1.96$  TeV. The dash-dotted curve corresponds to the LO, whereas the solid one to the NLO result. The uncertainty bands depict scale variation. The lower panels display the differential  $\mathcal{K}$  factor.

40%–50% corrections are visible at the tails of  $p_{T,j}$  spectrums, as compared to minus 20% in the low transverse momentum range.

And finally, in Figure 11, the invariant mass,  $m_{jj}$ , of the 1<sup>st</sup> and the 2<sup>nd</sup> hardest jet together with their separation in the  $(y, \phi)$  plane are shown. In both cases almost constant and rather moderate differential  $\mathcal{K}$ -factors

of 0.75 can be seen. Except for the tails of  $\Delta R_{jj}$  distribution where distortions are much higher. However, fluctuations visible there are a reflection of the limited statistics of the Monte Carlo integration. At the TeVatron,  $\Delta R_{jj}$  is dominated by the transverse plane peak at the begin of the spectrum, which suggests that two hardest jets are preferably produced almost collinear to



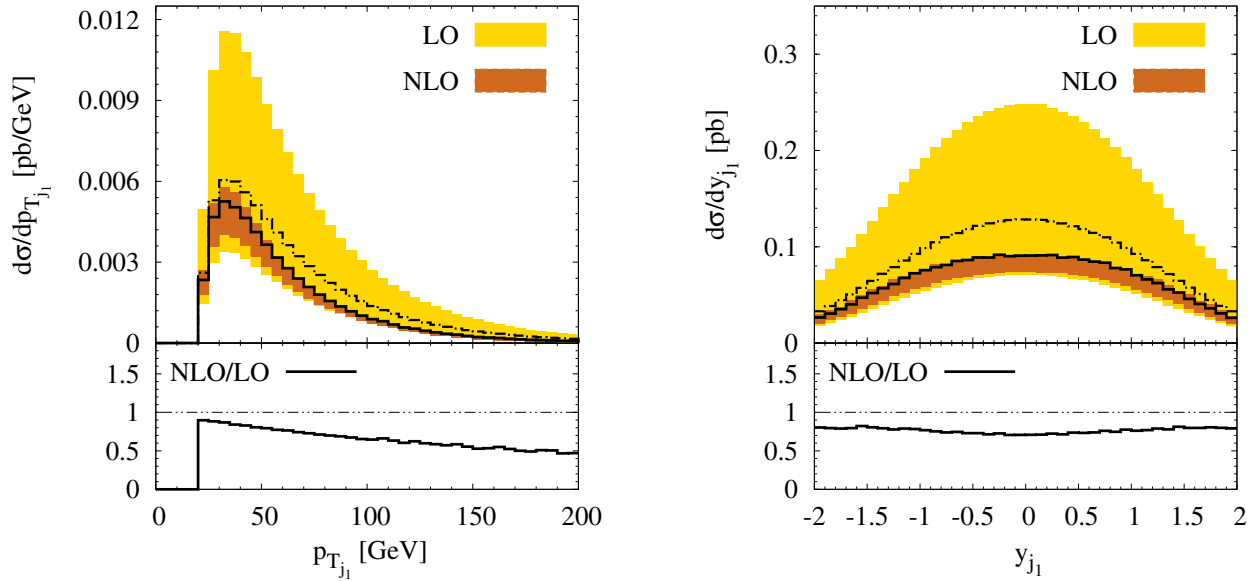


FIG. 9. Differential cross section distributions as a function of transverse momentum (left panel) and rapidity (right panel) of the 1st hardest jet for  $p\bar{p} \rightarrow t\bar{t}jj + X$  production at the TeVatron run II with  $\sqrt{s} = 1.96$  TeV. The dash-dotted curve corresponds to the LO, whereas the solid one to the NLO result. The uncertainty bands depict scale variation. The lower panels display the differential  $K$  factor.

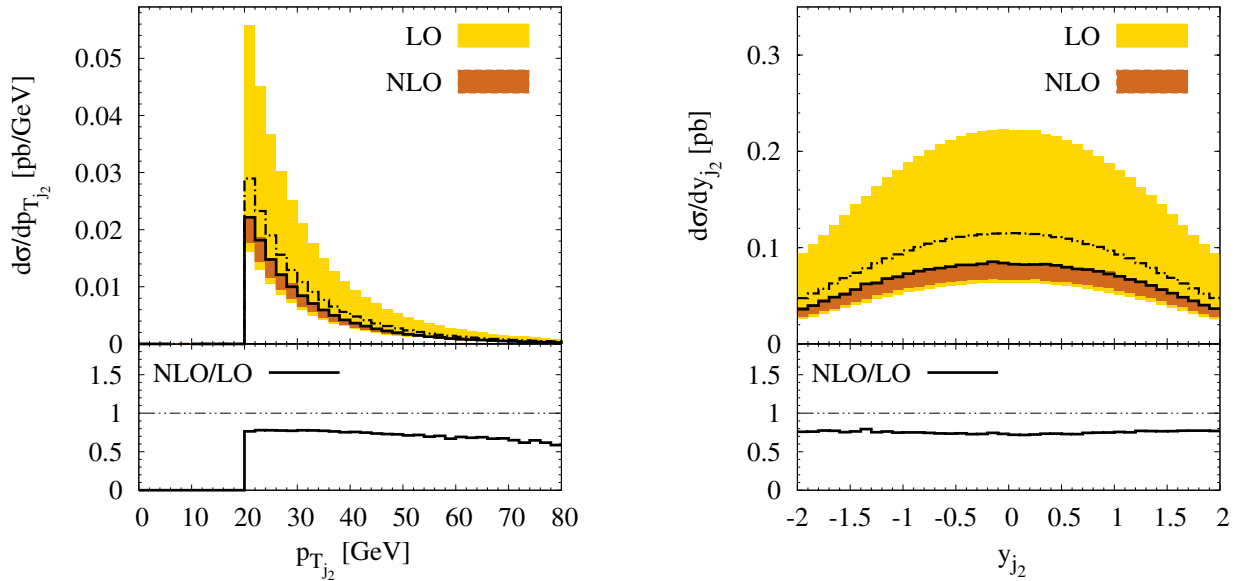


FIG. 10. Differential cross section distributions as a function of transverse momentum (left panel) and rapidity (right panel) of the 2nd hardest jet for  $p\bar{p} \rightarrow t\bar{t}jj + X$  production at the TeVatron run II with  $\sqrt{s} = 1.96$  TeV. The dash-dotted curve corresponds to the LO, whereas the solid one to the NLO result. The uncertainty bands depict scale variation. The lower panels display the differential  $K$  factor.

each other.

Overall, we can say that at the TeVatron employing a fixed scale  $\mu = \mu_R = \mu_F = m_t$ , the NLO corrections to transverse momentum distributions are rather substantial. Moreover, they do not simply rescale the LO shapes, but induce distortions at the level of 40%. The same applies to the invariant mass distribution of the  $t\bar{t}$  pair. In

case of the total transverse energy, even 50% – 60% deformations can be observed. For angular distributions and the invariant mass of two tagging jets we observe negative and rather moderate corrections of the order of 15% – 30%, which turn out to be relatively constant.

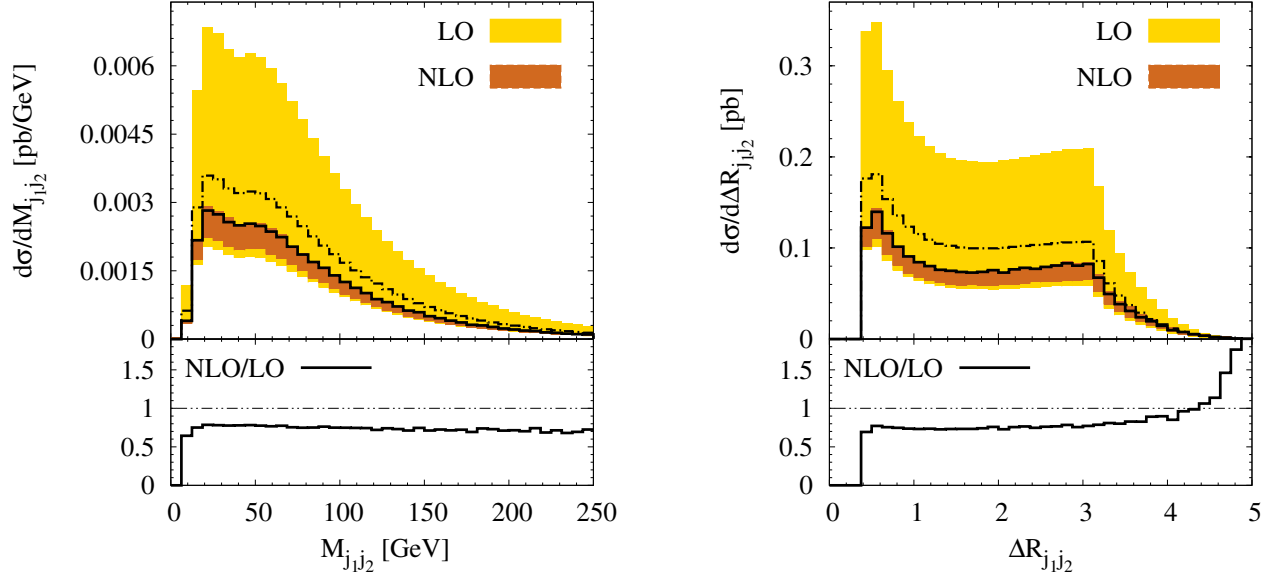


FIG. 11. Differential cross section distributions as a function of the invariant mass of the 1st and the 2nd hardest jet (left panel) and  $\Delta R_{jj}$  separation (right panel) for  $p\bar{p} \rightarrow t\bar{t}jj + X$  production at the TeVatron run II with  $\sqrt{s} = 1.96$  TeV. The dash-dotted curve corresponds to the LO, whereas the solid one to the NLO result. The uncertainty bands depict scale variation. The lower panels display the differential  $K$  factor.

TABLE VIII. Integrated cross sections at LO and NLO for  $pp \rightarrow t\bar{t}jj + X$  production at the LHC with  $\sqrt{s} = 7$  TeV. Results for three different jet algorithms are presented, the anti- $k_T$ ,  $k_T$  and the Cambridge/Aachen jet algorithms with  $R = 0.5$ . The scale choice is  $\mu_R = \mu_F = m_t$ .

CUTS	$\sigma_{\text{LO}}$ [pb]	$\sigma_{\text{NLO}}^{\text{anti-}k_T}$ [pb]	$\sigma_{\text{NLO}}^{k_T}$ [pb]	$\sigma_{\text{NLO}}^{C/A}$ [pb]
$p_{T_j} > 50$ GeV				
$\Delta R_{jj} > 0.5$	13.398(4)	9.82(2)	9.86(2)	9.86(2)
$ y_j  < 2.5$				

## B. LHC

As in the TeVatron case we calculate the partonic cross sections for events with at least two hard jets. Jets are obtained via the *anti- $k_T$*  jet algorithm with a resolution parameter  $R = 0.5$  and are required to have

$$p_{T_j} > 50 \text{ GeV}, \quad |y_j| < 2.5, \quad \Delta R_{jj} > 0.5. \quad (16)$$

We will refer to this set of cuts as *LHC default selection*. All results presented in this Section are given in picobarns.

### 1. Integrated cross sections

We turn now our attention to the LHC results. Let us stress here, that the cross sections and differential distributions presented in this section do not coincide with the

TABLE IX. Integrated cross section at LO and NLO for  $pp \rightarrow t\bar{t}jj + X$  production at the LHC with  $\sqrt{s} = 7$  TeV. Results for three different jet algorithms are presented, the anti- $k_T$ ,  $k_T$  and the Cambridge/Aachen jet algorithms with  $R = 1.0$ . The scale choice is  $\mu_R = \mu_F = m_t$ .

CUTS	$\sigma_{\text{LO}}$ [pb]	$\sigma_{\text{NLO}}^{\text{anti-}k_T}$ [pb]	$\sigma_{\text{NLO}}^{k_T}$ [pb]	$\sigma_{\text{NLO}}^{C/A}$ [pb]
$p_{T_j} > 50$ GeV				
$\Delta R_{jj} > 1.0$	11.561(4)	9.95(2)	10.06(2)	10.04(2)
$ y_j  < 2.5$				

TABLE X. Integrated cross section at NLO for  $pp \rightarrow t\bar{t}jj + X$  production at the LHC with  $\sqrt{s} = 7$  TeV. Results for two different values of the  $\alpha_{\text{max}}$  parameter and  $\Delta R_{jj}$  cut are presented. They are obtained with the *anti- $k_T$*  jet algorithm. The scale choice is  $\mu_R = \mu_F = m_t$ .

CUTS	$\sigma_{\text{NLO}}^{\alpha_{\text{max}}=0.01}$ [pb]	$\sigma_{\text{NLO}}^{\alpha_{\text{max}}=1.00}$ [pb]
$\Delta R_{jj} > 0.5, R = 0.5$	9.82(2)	9.81(1)
$\Delta R_{jj} > 1.0, R = 1.0$	9.95(2)	9.94(1)

ones shown in [11]. In the latter publication, a different center of mass energy,  $\sqrt{s} = 14$  TeV, has been assumed.

First, integrated cross sections with the LHC default selection as defined in the previous section, are provided. We obtain

$$\sigma_{\text{LO}}^{\text{LHC}}(pp \rightarrow t\bar{t}jj) = 13.398^{+11.713(87\%)}_{-5.788(43\%)} \text{ pb}, \quad (17)$$

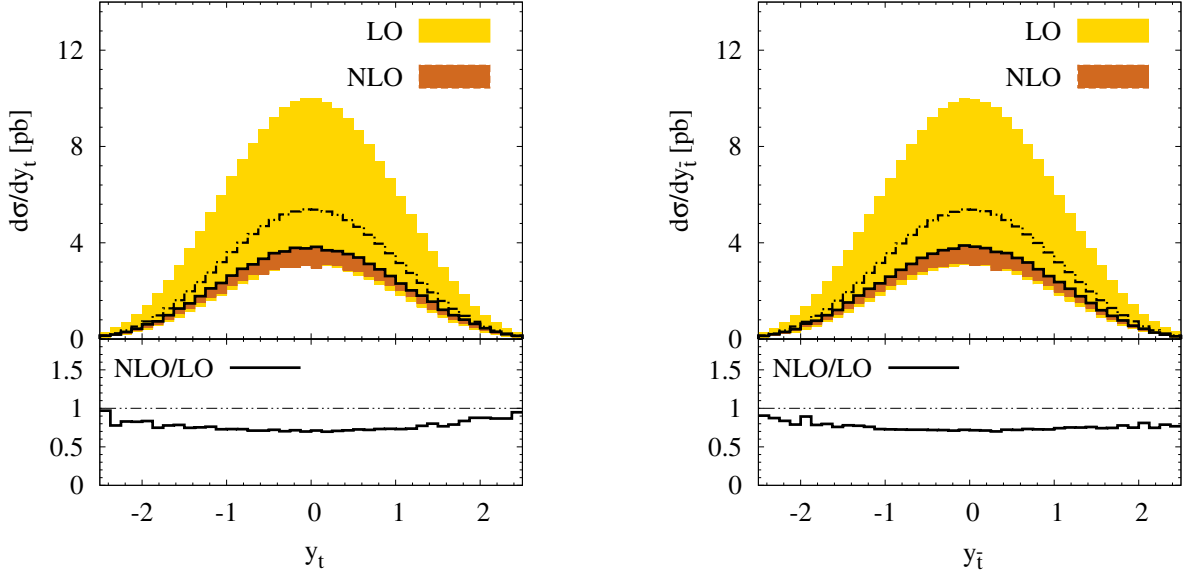


FIG. 12. Differential cross section distributions as a function of the rapidity of the top quark (left panel) and of the anti-top quark (right panel) for  $pp \rightarrow t\bar{t}jj + X$  production at the LHC with  $\sqrt{s} = 7$  TeV. The dash-dotted curve corresponds to the LO, whereas the solid one to the NLO result. The uncertainty bands depict scale variation. The lower panels display the differential  $\mathcal{K}$  factor.

TABLE XI. Integrated cross section at LO and NLO for  $pp \rightarrow t\bar{t}jj + X$  production at the LHC with  $\sqrt{s} = 7$  TeV. Results for the anti- $k_T$  jet algorithm with  $R = 0.5$  are presented. In the last two columns the  $\mathcal{K}$  factor, defined as the ratio of the NLO cross section to the respective LO result, and NLO corrections in % are given. The scale choice is  $\mu_R = \mu_F = m_t$ .

$p_{T_j}$ CUT	$\sigma_{\text{LO}}$ [pb]	$\sigma_{\text{NLO}}^{\text{anti-}k_T}$ [pb]	$\mathcal{K}$	[%]
$p_{T_j} > 50$ GeV	13.398(4)	9.82(2)	0.73	-27
$p_{T_j} > 75$ GeV	5.944(2)	4.115(8)	0.69	-31
$p_{T_j} > 100$ GeV	3.018(1)	1.944(4)	0.64	-36
$p_{T_j} > 125$ GeV	1.665(1)	0.993(2)	0.60	-40

$$\sigma_{\text{NLO}}^{\text{LHC}}(pp \rightarrow t\bar{t}jj) = 9.82^{+1.48(15\%)}_{-1.47(15\%)} \text{ pb}. \quad (18)$$

where the central value refers to  $\mu_R = \mu_F = m_t$ , the upper value to  $\mu = m_t/2$  and the lower value to  $\mu = 2m_t$ . At the central value of the scale the total cross section receives negative and moderate corrections of the order of 27%. Similar to the Tevatron case, the improvement in the scale stability at the NLO is prominent. The NLO cross section is very stable against changes in the renormalization and factorization scales, in contrary to the LO result where an 87% scale dependence is obtained.

As in the Tevatron case we have checked the effect coming from the jet algorithm variation. Results are presented in Table VIII. For the jet resolution parameter  $R = 0.5$  the difference between  $k_T$ , *anti* -  $k_T$  and the inclusive Cambridge/Aachen (C/A) jet finders is within 0.4%. With an increase of  $R$  values to  $R = 1.0$  the differ-

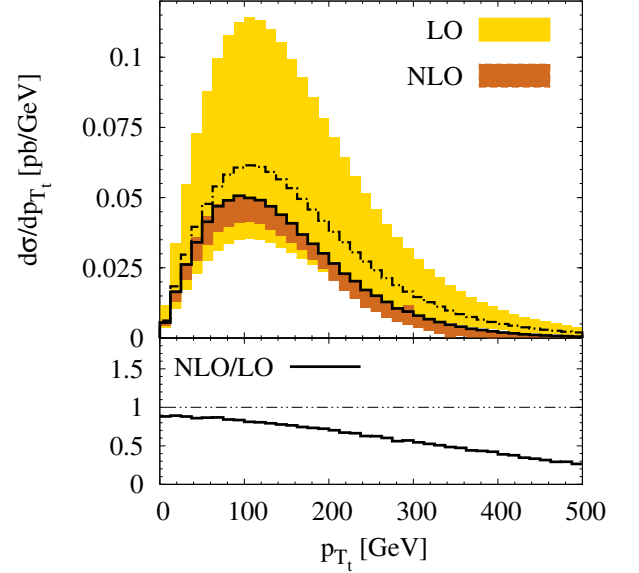


FIG. 13. Differential cross section distributions as a function of the averaged transverse momentum of the top and anti-top for  $pp \rightarrow t\bar{t}jj + X$  production at the LHC with  $\sqrt{s} = 7$  TeV. The dash-dotted curve corresponds to the LO, whereas the solid one to the NLO result. The uncertainty bands depict scale variation. The lower panels display the differential  $\mathcal{K}$  factor.

ence moves upwards to 1.1% as can be seen from Table IX. Moreover, for a higher jet separation cut  $\Delta R_{jj} > 1.0$  and a higher jet resolution parameter  $R = 1$ , NLO QCD

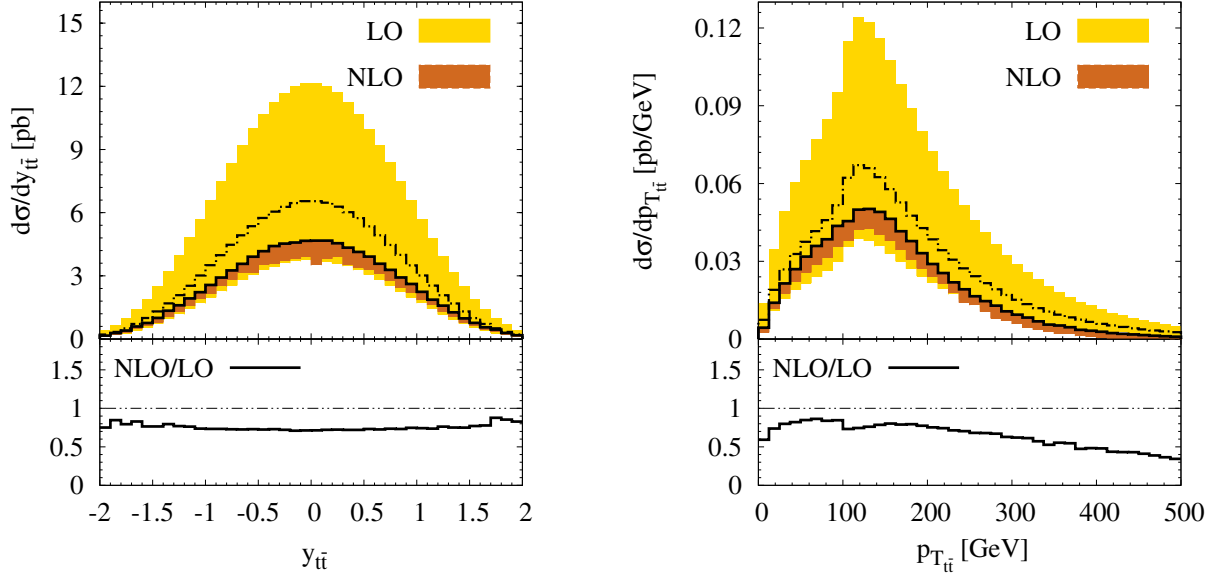


FIG. 14. Differential cross section distributions as a function of rapidity (left panel) and transverse momentum (right panel) of the  $t\bar{t}$  pair for  $pp \rightarrow t\bar{t}jj + X$  production at the LHC with  $\sqrt{s} = 7$  TeV. The dash-dotted curve corresponds to the LO, whereas the solid one to the NLO result. The uncertainty bands depict scale variation. The lower panels display the differential  $K$  factor.

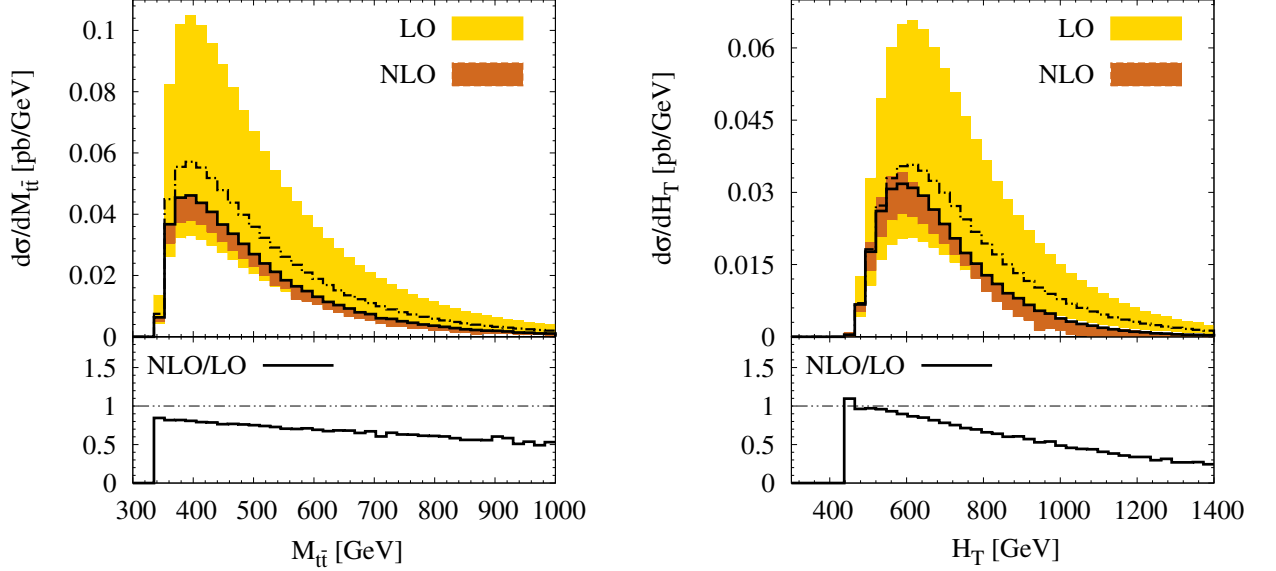


FIG. 15. Differential cross section distributions as a function of the invariant mass of the  $t\bar{t}$  pair (left panel) and of total transverse energy (right panel) for  $pp \rightarrow t\bar{t}jj + X$  production at the LHC with  $\sqrt{s} = 7$  TeV. The dash-dotted curve corresponds to the LO, whereas the solid one to the NLO result. The uncertainty bands depict scale variation. The lower panels display the differential  $K$  factor.

corrections are reduced down to  $-14\%$ . Again, the LO result scales down, this time by  $14\%$ , while in the NLO case we have an increase of the order of  $2\%$ . At LO one parton is equivalent to one jet, and the jet algorithm with size parameter  $R$  is equivalent to the requirement that any two partons should be separated by at least  $\Delta R_{jj}$  distance. A larger value of  $\Delta R_{jj}$  means smaller cross sections. At NLO, there can be two partons in a jet, and

jets may have some structure. A larger  $R$  means that the probability of radiation of a parton out of the area with interjet distance  $R$  is smaller. This can be translated into a reduced number of jets with  $p_T$  below the cut threshold and higher total NLO cross section. Contrary to the Tevatron case, this has not been overcome here by the simultaneous increase of the  $\Delta R_{jj}$  separation cut resulting in higher total NLO cross sections. At the

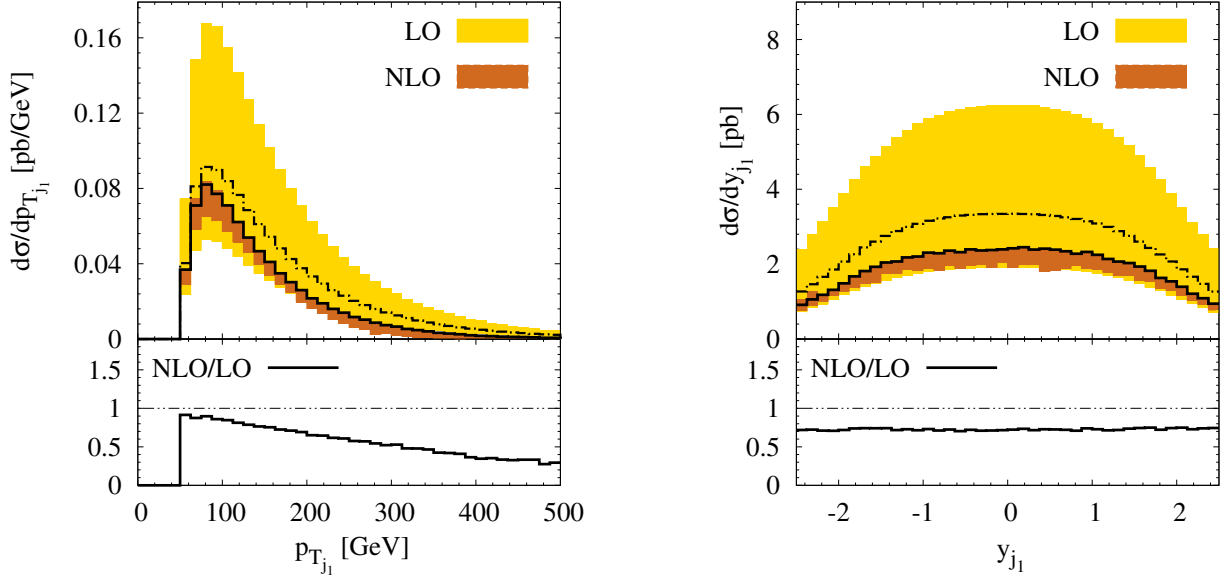


FIG. 16. Differential cross section distributions as a function of transverse momentum (left panel) and rapidity (right panel) of the 1st hardest jet for  $pp \rightarrow t\bar{t}jj + X$  production at the LHC with  $\sqrt{s} = 7$  TeV. The dash-dotted curve corresponds to the LO, whereas the solid one to the NLO result. The uncertainty bands depict scale variation. The lower panels display the differential  $\mathcal{K}$  factor.

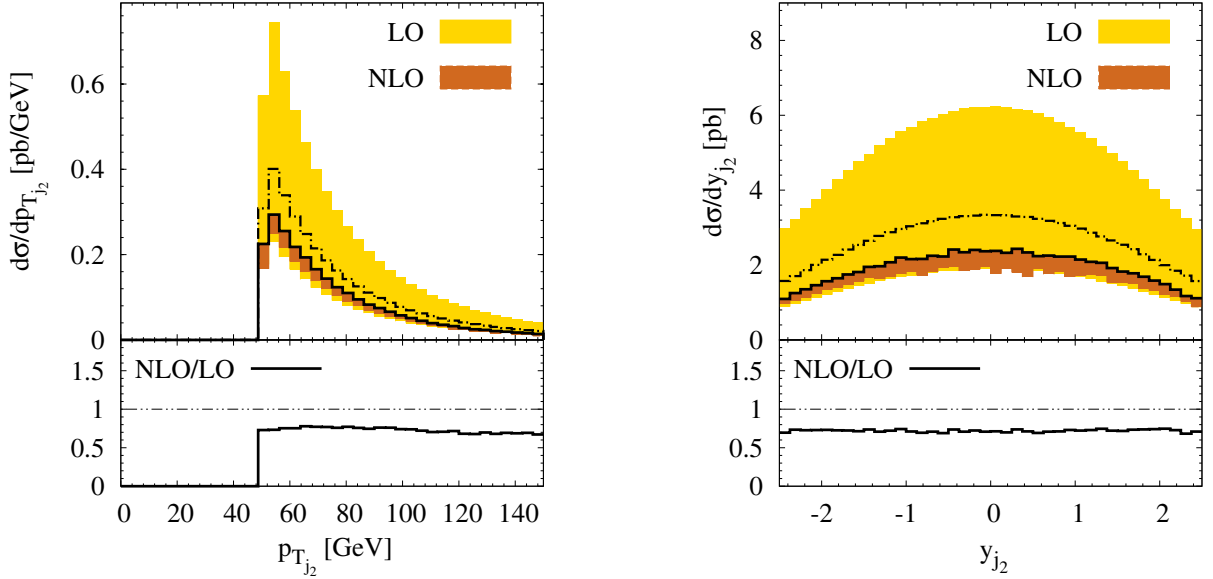


FIG. 17. Differential cross section distributions as a function of transverse momentum (left panel) and rapidity (right panel) of the 2nd hardest jet for  $pp \rightarrow t\bar{t}jj + X$  production at the LHC with  $\sqrt{s} = 7$  TeV. The dash-dotted curve corresponds to the LO, whereas the solid one to the NLO result. The uncertainty bands depict scale variation. The lower panels display the differential  $\mathcal{K}$  factor.

LHC, the two hard jets are more likely to be produced back-to-back. Therefore, events are mostly concentrated around  $\Delta R_{jj} = \pi$ , which is mildly affected by a change in  $\Delta R_{jj}$  cut from 0.5 to 1.

Similarly to the TeVatron case, NLO cross sections for two different values of the  $\alpha_{\max}$  parameter are given in Table X. The independence of the final result on  $\alpha_{\max}$  is

obtained again at the permil level.

In Table XI predictions for LO and NLO cross sections are presented with the default LHC selection, however, the transverse momentum cut of the two hard jets is varied between 50 GeV and 125 GeV. Within a 50 – 100 GeV range corrections are quite stable, changing the  $\mathcal{K}$  factor by less than 9%. For 125 GeV cut, we observed

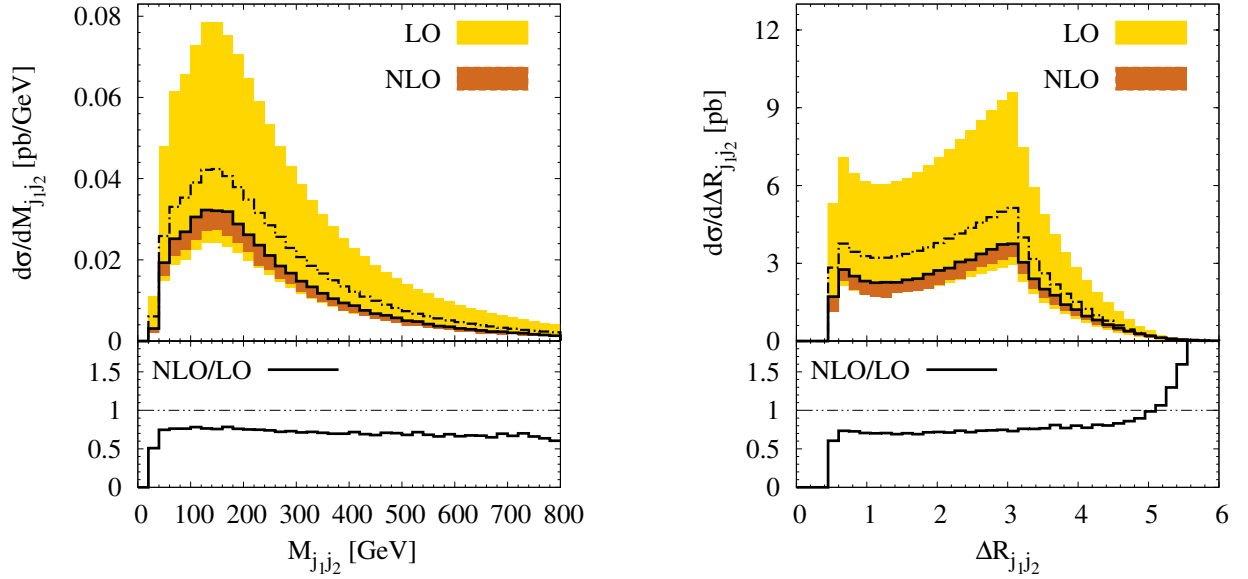


FIG. 18. Differential cross section distributions as a function of the invariant mass,  $m_{jj}$ , of the 1st and the 2nd hardest jet and  $\Delta R_{jj}$  separation for  $pp \rightarrow t\bar{t}jj + X$  production at the LHC with  $\sqrt{s} = 7$  TeV. The dash-dotted curve corresponds to the LO, whereas the solid one to the NLO result. The uncertainty bands depict scale variation. The lower panels display the differential  $\mathcal{K}$  factor.

a somehow higher rise of NLO QCD corrections up to  $-40\%$ . Compared to the total NLO  $t\bar{t}$  cross section,

$$\sigma_{\text{NLO}}^{\text{LHC}}(pp \rightarrow t\bar{t}) = 158.1^{+19.5(12\%)}_{-21.2(13\%)} \text{ pb}, \quad (19)$$

we discover that for the smallest  $p_{T_j}$  cut of 50 GeV the  $t\bar{t}jj$  events represent only 6% of the total cross section. The fraction is decreased to 3%, 1% and 0.6% for 75 GeV, 100 GeV and 125 GeV respectively.

## 2. Differential cross sections

In the following, we turn our attention to the size of the NLO QCD corrections to the differential distributions at the LHC with  $\sqrt{s} = 7$  TeV. For the LHC, a  $pp$  collider, the shapes of some distributions are quite different as compared to the TeVatron case. Top quark production at the LHC, for example, is forward-backward symmetric in the laboratory frame as a consequence of the symmetric initial state. Thus,  $\mathcal{A}_{\text{FB}}^t = \mathcal{A}_{\text{FB}}^{\bar{t}} = 0$ . This can be observed in Figure 12, where top and anti-top quark rapidity distributions, symmetric around  $y_t$ , are plotted at LO and NLO. Distributions get broadened, moving from the TeVatron to the LHC case, as can be expected from an increased scattering energy. On the other hand, the distribution in the averaged transverse momentum,  $p_{T_t}$ , of the top and anti-top, shown in Figure 13, becomes harder during this transition. Again, the dash-dotted curve corresponds to the LO, whereas the solid one to the NLO result. At LO the bands correspond to the choice of the renormalization and factorization scale

$\mu = m_t/2$  and  $\mu = 2m_t$ . In case of NLO they are determined out of the following set  $\mu = [m_t/2, m_t, 2m_t]$ . More precisely for each histogram, bands are constructed bin-by-bin, by calculating maximal and minimal values using the above three scales. Since the scale dependence of the NLO cross section at the LHC is a function that is not monotonic and the true maximum is somewhere close to the central value of the scale,  $m_t$ , this seems to be the only meaningful approach, if one is interested in plotting scale uncertainty bands without making a very costly scan. Let us emphasize here, that the scale variation is, by no means a rigorous way to estimate the theoretical uncertainty. At best, it might only give an indication of the full uncertainty which is due to the not yet calculated higher order corrections. The lower panels display the differential  $\mathcal{K}$  factor. Angular distributions exhibit negative corrections of the order of 30% in the central rapidity range and they are decreased to 20% at the forward and backward parts of the spectrum. As for the averaged transverse momentum distributions of the top and anti-top up to 60% distortions are observed.

In Figure 14 and Figure 15, differential cross section distributions as function of rapidity,  $y_{t\bar{t}}$ , transverse momentum,  $p_{T_{t\bar{t}}}$ , and the invariant mass,  $m_{t\bar{t}}$ , of the  $t\bar{t}$  pair are given. Furthermore, the total transverse energy of the system,  $H_T$ , is shown there. The rapidity distribution receives negative, but rather stable 25% corrections. Unlike  $p_{T_{t\bar{t}}}$ ,  $m_{t\bar{t}}$  and  $H_T$  spectrums, where distortions of the order of 50%, 35% and 80% respectively, are visible.

Subsequently, in Figure 16 and in Figure 17 differential cross section distributions as a function of transverse momentum,  $p_{T_j}$ , and rapidity,  $y_j$ , of the 1st and the 2nd



hardest jets are plotted. As anticipated for rapidity distributions, in both cases negative and quite stable corrections of the order of 30% appear. On the other hand, for the  $p_{T_{j_1}}$  spectrum, 60% distortions are obtained as compared to only 10% in  $p_{T_{j_2}}$  case.

Eventually, differential cross section distributions as a function of the dijet invariant mass,  $m_{jj}$ , are given in Figure 18. Also shown in Figure 18 is the separation in  $\Delta R_{jj}$  between two jets ordered in hardness. In both cases, rather constant  $-30\%$  corrections can be reached. Again, fluctuations visible at the tails of the  $\Delta R_{jj}$  distribution are caused by limited statistics of the Monte Carlo integration. As we can see at the LHC, the two hard jets are more likely to be produced back-to-back, leading to a more peaked distribution around  $\pi$ .

Generally, we can say that for a fixed scale  $\mu = \mu_R = \mu_F = m_t$  at the LHC, the NLO QCD corrections are always negative and protean. In case of angular distributions,  $y$ ,  $\Delta R$ , and the invariant mass distribution of the  $t\bar{t}$  pair, rather steady  $20\% - 30\%$  corrections are visible. In the transverse momentum distributions, on the other hand, they introduce up to 60% distortions. In addition, in the case of the total transverse energy,  $H_T$ , even 80% deformations can be observed.

#### IV. CONCLUSIONS

In this paper, we have presented a computation of the NLO QCD corrections to  $t\bar{t}$  pair production in association with two hard jets at the TeVatron and the LHC. The total cross sections and their scale dependence, as well as several differential distributions have been given. The NLO QCD corrections reduce the scale uncertainty of the total cross sections and of the differential distributions compared to LO calculations, which can only provide qualitative predictions.

In case of the TeVatron, the forward-backward asymmetry of the top quarks has been calculated for the first time. We have found that, with inclusive selection cuts, the forward-backward asymmetry amounts to  $\mathcal{A}_{\text{FB,LO}}^t = -10.3\%$  at LO and  $\mathcal{A}_{\text{FB,NLO}}^t = -4.6\%$  at NLO.

Furthermore, the impact of the NLO QCD corrections on integrated cross sections at the TeVatron is moderate, of the order of  $-24\%$ . At the LHC we have obtained NLO QCD corrections at the level of  $-27\%$ . In both cases, NLO QCD corrections are reduced substantially, if a higher jet resolution parameter  $R$  is chosen instead. Changing  $R$  from  $R = 0.4$  to  $R = 0.8$  in the TeVatron case and from  $R = 0.5$  to  $R = 1.0$  in the LHC case decreases NLO QCD corrections down to  $-16\%$  and  $-14\%$  respectively. A study of the scale dependence of our NLO predictions indicates that the residual theoretical uncertainty due to higher order corrections is 21% for the TeVatron and 15% for the LHC.

As a further matter, at the TeVatron employing a fixed scale  $\mu = \mu_R = \mu_F = m_t$ , the NLO corrections to differ-

ential distributions are negative and rather substantial. They do not simply rescale the LO shapes, but induce distortions up to 60%. Also in the LHC case the NLO QCD corrections to the distributions are always negative and protean. In the worst case even 80% deformations can be observed.

Finally, our paper demonstrates the utility of the off-shell methods and the OPP reduction procedure, as implemented in the HELAC-NLO system, in computing NLO QCD corrections for processes of phenomenological interest at hadron colliders. The system consists of, CUTTOOLS and HELAC-1LOOP which handle the virtual corrections and HELAC-DIPOLES for the real emission contributions. For the phase space integration the KALEU package is used and results are cross checked with the help of the PHEGAS phase space generator. Moreover, ONELOOP is deployed for the evaluation of the one-loop scalar functions. With this framework we can calculate NLO QCD corrections to the remaining multiparticle background and signal processes which are relevant in the ongoing analyzes at the TeVatron and at the LHC. Besides, we are prepared to compare NLO QCD predictions with already available data.

#### V. APPENDIX

In order to facilitate a comparison to our calculation, we provide values of the one-loop virtual corrections to the squared matrix elements for one phase space point which is given in Table XII. Virtual corrections come from the interference of the tree level and one-loop amplitudes, summed over all colors and spins, and for  $n_f = 5$  massless quark flavors. As mentioned before we describe the running of the strong coupling constant with two-loop accuracy, including five active flavors which corresponds to  $\alpha_s(m_t) = 0.109403691593462$  where  $m_t = 173.3$  GeV. In Table XIII we present numbers for all eight subprocesses. The quantities presented in Table XIII correspond to the renormalized virtual one-loop correction in the 't Hooft-Veltman [28] version of the dimensional regularization scheme. The remaining singularities in the dimensional regularization parameter  $d = 4 - 2\epsilon$  arise from the virtual soft and collinear singularities in the one-loop amplitudes. Additionally coefficients for color and spin summed results for the  $\mathcal{I}$ -operator of the dipole subtraction function as defined in [38] are presented. We can observe numerical cancellations of infrared divergences between the  $\mathcal{I}$ -operator and the corresponding virtual contributions at least up to 10 digits.

#### ACKNOWLEDGMENTS

The calculations have been performed on the Grid Cluster of the Bergische Universität Wuppertal, financed by the Helmholtz - Alliance "Physics at the Terascale" and the BMBF.

TABLE XII. The set of momenta for  $12 \rightarrow t\bar{t}34$  process with the notation  $(p_x, p_y, p_z, E)$  and all the components given in GeV. The top quark mass is set to  $m_t = 173.3$  GeV.

PARTON	$p_x$	$p_y$	$p_z$	E
$p_1$	0	0	2424.746502697520	2424.746502697520
$p_2$	0	0	-2424.746502697520	2424.746502697520
$p_t$	-715.3340594013138	-475.1625187999429	101.1925816377932	881.9042263139404
$p_{\bar{t}}$	-24.14783219601748	-6.328336607570634	295.5085181344487	343.4841188963524
$p_3$	21.87826794850173	1000.411563795763	1341.334408905234	1673.463460042633
$p_4$	717.6036236488295	-518.9207083882493	-1738.035508677476	1950.641200142114

TABLE XIII. Numerical values of the virtual corrections to the squared matrix elements at the phase space point given in Table XII and  $\mu_R = \mu_F = m_t$  for all the partonic subprocesses for the  $t\bar{t}jj$  production at a hadron collider. We give the finite parts along with the coefficients of the poles in  $\epsilon$ . Additionally coefficients for color and spin summed results for the  $\mathcal{I}$ -operator are presented.

SUBPROCESS	$1/\epsilon^2$	$1/\epsilon$	$1/\epsilon^0$
$gg \rightarrow t\bar{t}gg$	$-4.759403785663033 \times 10^{-9}$	$1.868033206671699 \times 10^{-8}$	$-3.727507250164706 \times 10^{-8}$
$\mathcal{I}(\epsilon)$	$4.759403785663084 \times 10^{-9}$	$-1.868033206665652 \times 10^{-8}$	
$gg \rightarrow t\bar{t}u\bar{u}$	$-1.243597961079720 \times 10^{-11}$	$4.205081694102065 \times 10^{-11}$	$-8.435931194456964 \times 10^{-11}$
$\mathcal{I}(\epsilon)$	$1.243597961079740 \times 10^{-11}$	$-4.205081694097688 \times 10^{-11}$	
$u\bar{u} \rightarrow t\bar{t}gg$	$-3.408532130149515 \times 10^{-11}$	$1.296674677886268 \times 10^{-10}$	$-2.908105638419785 \times 10^{-10}$
$\mathcal{I}(\epsilon)$	$3.408532130149502 \times 10^{-11}$	$-1.296674677886843 \times 10^{-10}$	
$u\bar{u} \rightarrow t\bar{t}u\bar{u}$	$-5.610006218609934 \times 10^{-10}$	$3.140716653723494 \times 10^{-9}$	$-6.264131939313179 \times 10^{-9}$
$\mathcal{I}(\epsilon)$	$5.610006218609923 \times 10^{-10}$	$-3.140716653723457 \times 10^{-9}$	
$ug \rightarrow t\bar{t}ug$	$-2.178331428688374 \times 10^{-9}$	$9.512663847206611 \times 10^{-9}$	$-1.925455596882764 \times 10^{-8}$
$\mathcal{I}(\epsilon)$	$2.178331428688390 \times 10^{-9}$	$-9.512663847144086 \times 10^{-9}$	
$gu \rightarrow t\bar{t}ug$	$-5.212043686490916 \times 10^{-11}$	$1.749451737240981 \times 10^{-10}$	$-3.143378807927551 \times 10^{-10}$
$\mathcal{I}(\epsilon)$	$5.212043686491147 \times 10^{-11}$	$-1.749451737238111 \times 10^{-10}$	
$ud \rightarrow t\bar{t}ud$	$-5.488979123409352 \times 10^{-10}$	$3.020380070883476 \times 10^{-9}$	$-5.979795310554041 \times 10^{-9}$
$\mathcal{I}(\epsilon)$	$5.488979123409385 \times 10^{-10}$	$-3.020380070883462 \times 10^{-9}$	
$u\bar{u} \rightarrow t\bar{t}d\bar{d}$	$-2.663317234536143 \times 10^{-13}$	$1.278242588447108 \times 10^{-12}$	$-4.283899547423337 \times 10^{-12}$
$\mathcal{I}(\epsilon)$	$2.663317234536076 \times 10^{-13}$	$-1.278242588446499 \times 10^{-12}$	

M. Czakon was supported by the Heisenberg and by the Gottfried Wilhelm Leibniz Programmes of the Deutsche Forschungsgemeinschaft and M. Worek by the Initiative and Networking Fund of the Helmholtz Asso-

ciation, contract HA-101 (“Physics at the Terascale”).

M. Worek would also like to thank German Rodrigo for helpful discussions.

[1] G. Aad *et al.* [The ATLAS Collaboration], *Expected Performance of the ATLAS Experiment - Detector, Trigger*

*and Physics*, [arXiv:0901.0512 [hep-ex]].

- [2] G. L. Bayatian *et al.* [CMS Collaboration], *CMS technical design report, volume II: Physics performance*, J. Phys. G **34** (2007) 995.
- [3] S. Asai *et al.*, *Prospects for the search for a standard model Higgs boson in ATLAS using vector boson fusion*, Eur. Phys. J. C **32S2**, 19 (2004), [arXiv:hep-ph/0402254].
- [4] T. Aaltonen *et al.* [CDF and D0 Collaboration], *Combined CDF and D0 Upper Limits on Standard Model Higgs Boson Production with up to  $8.2 \text{ fb}^{-1}$  of Data*, [arXiv:1103.3233 [hep-ex]].
- [5] Andrey Korytov, on behalf of the CMS Collaboration, *Combined results on SM Higgs Search with the CMS Detector*, International Europhysics Conference on High-Energy Physics, (EPS-HEP 2011), Grenoble, France, 21-27 July 2011, <http://eps-hep2011.eu/>.
- [6] Kyle Cranmer, on behalf of the ATLAS Collaboration, *Combined ATLAS Standard Model Higgs Search with  $1 \text{ fb}^{-1}$  of Data at 7 TeV*, International Europhysics Conference on High-Energy Physics, (EPS-HEP 2011), Grenoble, France, 21-27 July 2011, <http://eps-hep2011.eu/>.
- [7] A. Bredenstein, A. Denner, S. Dittmaier and S. Pozzorini, *NLO QCD corrections to  $pp \rightarrow t\bar{t}b\bar{b} + X$  at the LHC*, Phys. Rev. Lett. **103**, 012002 (2009), [arXiv:0905.0110 [hep-ph]].
- [8] G. Bevilacqua, M. Czakon, C. G. Papadopoulos, R. Pittau and M. Worek, *Assault on the NLO Wishlist:  $pp \rightarrow t\bar{t}b\bar{b}$* , JHEP **0909** (2009) 109, [arXiv:0907.4723 [hep-ph]].
- [9] A. Bredenstein, A. Denner, S. Dittmaier and S. Pozzorini, *NLO QCD corrections to top anti-top bottom anti-bottom production at the LHC: 2. full hadronic results*, JHEP **1003**, 021 (2010), [arXiv:1001.4006 [hep-ph]].
- [10] T. Melia, K. Melnikov, R. Rontsch and G. Zanderighi, *NLO QCD corrections for  $W^+W^-$  pair production in association with two jets at hadron colliders*, Phys. Rev. D **83**, 114043 (2011), [arXiv:1104.2327 [hep-ph]].
- [11] G. Bevilacqua, M. Czakon, C. G. Papadopoulos and M. Worek, *Dominant QCD Backgrounds in Higgs Boson Analyses at the LHC: A Study of  $pp \rightarrow t\bar{t} + 2 \text{ jets}$  at Next-To-Leading Order*, Phys. Rev. Lett. **104** (2010) 162002, [arXiv:1002.4009 [hep-ph]].
- [12] G. Bevilacqua, M. Czakon, A. van Hameren, C. G. Papadopoulos and M. Worek, *Complete off-shell effects in top quark pair hadroproduction with leptonic decay at next-to-leading order*, JHEP **1102** (2011) 083, [arXiv:1012.4230 [hep-ph]].
- [13] P. Draggiotis, R. H. P. Kleiss and C. G. Papadopoulos, *On the computation of multigluon amplitudes*, Phys. Lett. B **439** (1998) 157, [arXiv:hep-ph/9807207].
- [14] P. D. Draggiotis, R. H. P. Kleiss and C. G. Papadopoulos, *Multijet production in hadron collisions*, Eur. Phys. J. C **24** (2002) 447, [arXiv:hep-ph/0202201].
- [15] M. Czakon, C. G. Papadopoulos and M. Worek, *Polarizing the Dipoles*, JHEP **0908** (2009) 085, [arXiv:0905.0883 [hep-ph]].
- [16] A. Kanaki and C. G. Papadopoulos, *HELAC: A package to compute electroweak helicity amplitudes*, Comput. Phys. Commun. **132** (2000) 306, [hep-ph/0002082].
- [17] C. G. Papadopoulos, *PHEGAS: A phase space generator for automatic cross section computation*, Comput. Phys. Commun. **137** (2001) 247, [hep-ph/0007335].
- [18] A. Cafarella, C. G. Papadopoulos and M. Worek, *Helac-Phegas: a generator for all parton level processes*, Comput. Phys. Commun. **180** (2009) 1941, [arXiv:0710.2427 [hep-ph]].
- [19] T. Gleisberg, F. Krauss, C. G. Papadopoulos, A. Schaelicke and S. Schumann, *Cross sections for multi-particle final states at a linear collider*, Eur. Phys. J. C **34** (2004) 173, [hep-ph/0311273].
- [20] C. G. Papadopoulos and M. Worek, *Multi-parton Cross Sections at Hadron Colliders*, Eur. Phys. J. C **50** (2007) 843, [hep-ph/0512150].
- [21] J. Alwall *et al.*, *Comparative study of various algorithms for the merging of parton showers and matrix elements in hadronic collisions*, Eur. Phys. J. C **53** (2008) 473, [arXiv:0706.2569 [hep-ph]].
- [22] C. Englert, B. Jager, M. Worek and D. Zeppenfeld, *Observing Strongly Interacting Vector Boson Systems at the CERN Large Hadron Collider*, Phys. Rev. D **80** (2009) 035027, [arXiv:0810.4861 [hep-ph]].
- [23] S. Actis *et al.*, *Quest for precision in hadronic cross sections at low energy: Monte Carlo tools vs. experimental data*, Eur. Phys. J. C **66** (2010) 585, [arXiv:0912.0749 [hep-ph]].
- [24] C. C. Calame *et al.*, *NNLO leptonic and hadronic corrections to Bhabha scattering and luminosity monitoring at meson factories*, JHEP **1107**, 126 (2011), [arXiv:1106.3178 [hep-ph]].
- [25] A. van Hameren, *PARNI for importance sampling and density estimation*, Acta Phys. Polon. B **40** (2009) 259, [arXiv:0710.2448 [hep-ph]].
- [26] A. van Hameren, *Kaleu: a general-purpose parton-level phase space generator*, arXiv:1003.4953 [hep-ph].
- [27] P. Nogueira, *Automatic Feynman graph generation*, J. Comput. Phys. **105** (1993) 279.
- [28] G. 't Hooft and M. J. G. Veltman, *Regularization and Renormalization of Gauge Fields*, Nucl. Phys. B **44** (1972) 189.
- [29] A. van Hameren, C. G. Papadopoulos and R. Pittau, *Automated one-loop calculations: a proof of concept*, JHEP **0909** (2009) 106, [arXiv:0903.4665 [hep-ph]].
- [30] G. Ossola, C. G. Papadopoulos and R. Pittau, *Reducing full one-loop amplitudes to scalar integrals at the integrand level*, Nucl. Phys. B **763** (2007) 147, [hep-ph/0609007].
- [31] G. Ossola, C. G. Papadopoulos and R. Pittau, *CutTools: a program implementing the OPP reduction method to compute one-loop amplitudes*, JHEP **0803** (2008) 042, [arXiv:0711.3596 [hep-ph]].
- [32] P. Draggiotis, M. V. Garzelli, C. G. Papadopoulos and R. Pittau, *Feynman Rules for the Rational Part of the QCD 1-loop amplitudes*, JHEP **0904** (2009) 072, [arXiv:0903.0356 [hep-ph]].
- [33] M. V. Garzelli, I. Malamos and R. Pittau, *Feynman rules for the rational part of the Electroweak 1-loop amplitudes*, JHEP **1001** (2010) 040, [Erratum-ibid. **1010** (2010) 097], [arXiv:0910.3130 [hep-ph]].
- [34] M. V. Garzelli, I. Malamos and R. Pittau, *Feynman rules for the rational part of the Electroweak 1-loop amplitudes in the  $R_\xi$  gauge and in the Unitary gauge*, JHEP **1101** (2011) 029, [arXiv:1009.4302 [hep-ph]].
- [35] M. V. Garzelli and I. Malamos, *R2SM: A Package for the analytic computation of the  $R_2$  Rational terms in the Standard Model of the Electroweak interactions*, Eur. Phys. J. C **71** (2011) 1605, [arXiv:1010.1248].

- [hep-ph]].
- [36] A. van Hameren, *OneLoop: for the evaluation of one-loop scalar functions*, [arXiv:1007.4716 [hep-ph]].
  - [37] S. Catani and M. H. Seymour, *A general algorithm for calculating jet cross sections in NLO QCD*, Nucl. Phys. **B485** (1997) 291, [hep-ph/9605323].
  - [38] S. Catani, S. Dittmaier, M. H. Seymour and Z. Trocsanyi, *The dipole formalism for next-to-leading order QCD calculations with massive partons*, Nucl. Phys. **B627** (2002) 189, [hep-ph/0201036].
  - [39] A. D. Martin, W. J. Stirling, R. S. Thorne and G. Watt, *Parton distributions for the LHC*, Eur. Phys. J. C **63** (2009) 189, [arXiv:0901.0002 [hep-ph]].
  - [40] CDF and D0 Collaboration, *Combination of CDF and D0 Results on the Mass of the Top Quark using up to 5.6 fb<sup>-1</sup> of data*, [arXiv:1007.3178 [hep-ex]].
  - [41] S. Catani, Y. L. Dokshitzer and B. R. Webber, *The k-perpendicular clustering algorithm for jets in deep inelastic scattering and hadron collisions*, Phys. Lett. **B285** (1992) 291.
  - [42] S. Catani, Y. L. Dokshitzer, M. H. Seymour and B. R. Webber, *Longitudinally invariant k<sub>T</sub> clustering algorithms for hadron hadron collisions*, Nucl. Phys. **B406** (1993) 187.
  - [43] S. D. Ellis and D. E. Soper, *Successive combination jet algorithm for hadron collisions*, Phys. Rev. **D48** (1993) 3160, [hep-ph/9305266].
  - [44] M. Cacciari, G. P. Salam and G. Soyez, *The anti-k<sub>T</sub> jet clustering algorithm*, JHEP **0804** (2008) 063, [arXiv:0802.1189 [hep-ph]].
  - [45] Y. L. Dokshitzer, G. D. Leder, S. Moretti and B. R. Webber, *Better Jet Clustering Algorithms*, JHEP **9708** (1997) 001, [hep-ph/9707323].
  - [46] S. Dittmaier, P. Uwer and S. Weinzierl, *NLO QCD corrections to t anti-t + jet production at hadron colliders*, Phys. Rev. Lett. **98** (2007) 262002, [arXiv:hep-ph/0703120].
  - [47] S. Dittmaier, P. Uwer and S. Weinzierl, *Hadronic top-quark pair production in association with a hard jet at next-to-leading order QCD: Phenomenological studies for the Tevatron and the LHC*, Eur. Phys. J. C **59** (2009) 625, [arXiv:0810.0452 [hep-ph]].